Separation and Purification Technology 389 (2026) 136751

Contents lists available at ScienceDirect

Separation and Purification Technology

journal homepage: www.elsevier.com/locate/seppur

# Microwave-assisted desorption of $CO_2$ from ethanolamine solvent in a porous hollow fiber membrane - numerical modeling

A. Hajj [a,c], S. Curet [b], P. Pré [a,*]

[a] IMT Atlantique, GEPEA, UMR CNRS 6144, 44307 Nantes, France
[b] Oniris, Nantes Université, CNRS, GEPEA, UMR 6144, F-44000 Nantes, France
[c] SAIREM, 82, rue Elisée Reclus, 69150 Decines Charpieu, France

ARTICLE INFO

Editor: Yeshui Zhang

*Keywords:*
Microwave
Solvent regeneration
Desorption
$CO_2$ capture
Process electrification
Membrane

ABSTRACT

In our previous work, microwave regeneration of 30 wt% ethanolamine solvents in a hollow fiber gas-liquid contactor was experimentally investigated. In this system, the $CO_2$ desorption process was operated as the solvent was heated by microwaves when flowing through the lumen of the hollow fiber. Experimental results do not provide insight into the effect of microwaves on the regeneration performances. The aim of this study is therefore to develop a model to simulate the microwave solvent regeneration in the single fiber system.

The numerical approach is based on coupling 3D microwave heating of solvent flow, and 1D chemical desorption of $CO_2$ applicable to non-isothermal conditions along the fiber. The model was successful in reproducing with reasonable accuracy the global desorption data from the regeneration experiments, assuming a low wetting fraction of the membrane. The effects of operating conditions were explored: results show that increasing the solvent flow rates induces higher temperature gradients at the boundary of the fiber lumen thus increasing desorption rates. It has been found that increased fiber radius leads to better desorption rates at the expense of lowering the interfacial surface density. On another note, numerical results show that isothermal regeneration performs better than microwave mode although the latter is able to outperform where hotspots persist along the fiber. With regards to flow configurations during microwave regeneration, counter-current mode performed better than co-current one: the sweeping gas in the former mode passes from the hot solvent side to the cold solvent side which encourages reabsorption of the desorbed $CO_2$.

## 1. Introduction

Since the industrial revolution, human activity has increased greenhouse gases (GHG), causing global warming and risks like heat-related deaths, biodiversity loss (forests, coral reefs, arctic), reduced food production, freshwater scarcity [1], and coastal migration due to sea level rise [2,3]. The Paris Agreement (2015, COP 21) seeks to limit warming below 2 °C or ideally 1.5 °C by 2050 through net-zero emissions [4]. To allow for the continual use of fossil fuel while conforming to net-zero emissions, carbon capture allows decoupling emissions from the fuel type used. Perhaps the category of carbon capture that is the most advanced is the Post-combustion capture (PCC) technologies [5] and more specifically amine absorption. Historically, amine absorption process employs aqueous ethanolamine (ETA) [6] for the separation of $CO_2$ from natural gas. It was fitted to capture $CO_2$ from flue gases at a rate of 80–95 % [7,8]. Associated to this technology are elevated capital expenditures and high energetic costs that inhibit wide-scale deployment [9,10].

Advances in amine absorption include but are not limited to novel gas-liquid contactors such as polymeric membranes, or microwave irradiation as a heat source. The use of membranes in amine absorption was first proposed in 1980s for the absorption of $CO_2$ in sodium hydroxide solution [11,12]. The membrane acts as a non-selective barrier between gas and liquid phases, and its use is motivated by many advantages [13–16] such as: high interfacial surface densities- up to 30 times [17], modularity, increased operational flexibility [18]. On the other hand, microwave (MW) heating has found many applications in the chemical industry [19]: organic synthesis [20,21], heterogeneous catalysis [22] or MW-assisted extraction [23]. Advantages of this heating mode include higher energetic efficiency [24,25], shortening the treatment time (up to 50 %) [26], selective and volumetric heating rates. Having said that, it is of high interest to investigate the potential of using

* Corresponding author.
*E-mail address:* Pascaline.Pre@imt-atlantique.fr (P. Pré).

https://doi.org/10.1016/j.seppur.2026.136751
Received 2 October 2025; Received in revised form 15 December 2025; Accepted 2 January 2026
Available online 5 January 2026
1383-5866/© 2026 The Author(s). Published by Elsevier B.V. This is an open access article under the CC BY license (http://creativecommons.org/licenses/by/4.0/).

microwave (MW) heating for regenerating aqueous 30 %wt ETA solution loaded with dissolved $CO_2$, all while utilizing a hollow fiber membrane as a gas-liquid contactor. Using hollow fiber membranes for microwave solvent regeneration offers the benefits of membrane processes, and enables continuous operation contrary to others which operated in batch-mode [27–29]. One notable advantage of hollow fibers is the stable interfacial areas and simple fluid dynamics, paving the way for future modeling and a greater understanding of the effects of microwaves on desorption process.

In our previous work, microwave regeneration of $CO_2$ from 30 wt% ethanolamine solution was studied in a hollow fiber gas-liquid contactor. In that work, the regeneration performance was characterized as a function of the operating conditions, and comparison with literature data provided an initial assessment of the separation performance. The experimental work measured the global desorption rates and give a mere bird's-view perspective on the process, not providing any details or insights into the mass and heat transfers controlling this process. It is therefore clear that a numerical modeling approach is in order. In this work, we present the development of a multi-physical model that simulates chemical desorption of $CO_2$ from an alkanolamine solution in a millimetric hollow fiber placed inside a mono-mode microwave applicator. A progressive complexification strategy was adopted in order to couple the electromagnetic field propagation with the heat and mass transfer phenomena governing the chemical desorption process. We start by simulating the propagation of the electromagnetic fields in the microwave applicator; afterwards, heat and momentum transfers were integrated into the model to simulate the microwave heating process of a laminar flow of the solvent in the hollow fiber. In parallel, a resistance-in-series model was adopted to simulate chemical desorption of $CO_2$ in a hollow fiber membrane under condition of partial wetting of the porous matrix and non-isothermal conditions. The coupling between the 3D-MW heating model and the 1D transfer model allows the quantification of the local desorption rates as a function of the fiber length. The model was validated against experimental data and used to examine the influence of varying operating conditions on desorption flux, such as fiber size, co-current versus counter-current modes. The model sensitivity with respect to parameters representative of membrane and transfer properties was also assessed.

## 2. Experimental system: A hollow fiber membrane in a mono-mode microwave applicator

In previous part of the present work, microwave regeneration tests were carried out using the set-up shown in Fig. 2-1. A hollow fiber was fixed concentrically in a quartz tube and the ensemble was placed in a standard waveguide section (WR340) parallel to the small dimension (43 mm). The solvent which is 30 wt% ETA aqueous solution, enriched with $CO_2$, was made to circulate inside the fiber lumen at an entry temperature $T_{in}$ = 20 °C, and exiting at $T_{out}$. On the annular side between the fiber and the quartz tube a $N_2$ flow played the role of sweeping gas. During operation MWs traverse the waveguide under the fundamental mode ($TE_{10}$) until they reach the applicator and get absorbed by the solvent. The temperature increase of the latter evokes desorption; $CO_2$ concentration is quantified by an infrared sensor. Experimental global desorption rates ($J_{avg}$) were determined as a function of the operating conditions, in the framework of ($2^k$) plan of experimental design. Operating conditions of interest include: the carbonation ratio (α), outlet temperature of solvent ($T_{out}$), the solvent ($v_l$) and gas ($v_g$) volumetric flow rates. The total number of experimental points tested reached 16 experiments.

## 3. Modeling electromagnetic field propagation in the mono-mode applicator

To describe the propagation of the electromagnetic fields in the applicator, Maxwell's equations need to be solved over the representative domain. Maxwell's equations are reminded in equations ((3–1)-((3–4) for ease of reference, with ($\vec{E}_s$) and ($\vec{H}_s$) being the electric and magnetic field intensities represented in phasor form, (ε) being the electric permittivity, (μ) the magnetic permeability, (σ) being the direct current (DC) electrical conductivity of the material, and (ω) being the angular frequency.

Gauss's law $\nabla.\vec{E_s} = 0$ (3-1)

Magnetic monopole $\nabla.\overrightarrow{H_s} = 0$ (3-2)

Faraday's law $\nabla \times \vec{E_s} = -j\omega\mu\overrightarrow{H_s}$ (3-3)

Ampere – Maxwell law $\nabla \times \overrightarrow{H_s} = (\sigma + j\omega\varepsilon)\vec{E_s}$ (3-4)

### 3.1. Geometry and boundary conditions

The domain representative of the experimental system for solvent regeneration at the fiber scale is shown in Fig. 3-1. The domain includes

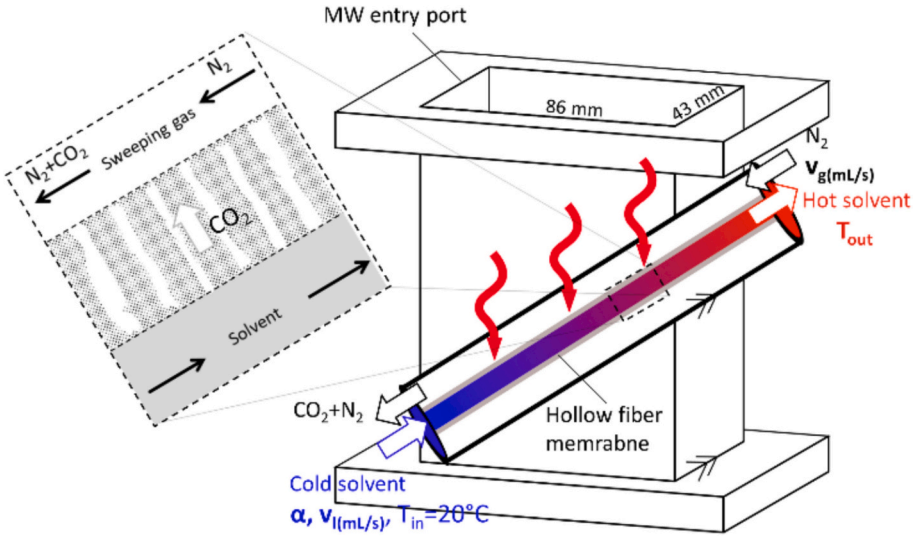



**Fig. 2-1.** Representation of the experimental system used to perform microwave regeneration tests of $CO_2$-rich 30 wt% ETA solvent in a hollow fiber. Operating conditions include: α, $T_{out}$, $v_l$, $v_g$.

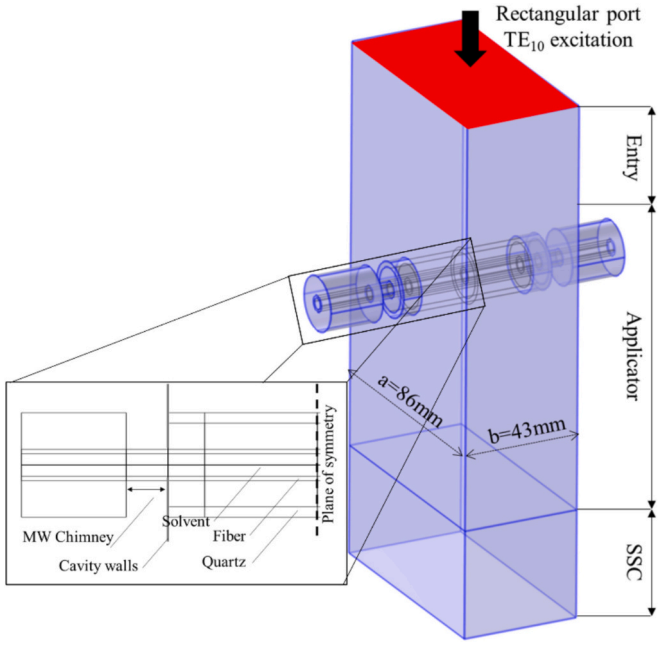



**Fig. 3-1.** Representation of the modeled MW-assisted desorption system in Comsol multi-physics.

the MW entry port, the applicator and the sliding short circuit (SSC). The microwave applicator is composed of a PTFE hollow fiber oriented in parallel with respect to the incident *E*-field at the entry port. The fiber is placed concentrically with respect to a surrounding quartz tube where desorbed $CO_2$ is collected and diluted in a stream of $N_2$-gas.

The propagation of electromagnetic fields was simulated using the software Comsol® Multiphysics (6.1). The physical module "Radio Frequency" was used to simulate EM field propagation over the entire modeled domain by solving Maxwell's equations. Fig. 3-1 shows the model geometry, the port is excited by a ($TE_{10}$), The walls of the waveguide are assumed to be a perfect electric conductor (PEC), hence the tangential component of the *E*-field cannot exist in that neighborhood ($\vec{n} \times \vec{E} = 0$).

The dielectric properties of the materials composing the gas-liquid contactor used in the simulation environment are given in Table 3-1. The dielectric properties of fused quartz and PTFE were obtained from the book of Von Hippel [30], while those of the porous fiber were derived by using the Landau-Lifshitz-Looyenga dielectric mixing law [31]. The properties of distilled water and loaded 30 wt% ETA are obtained from the correlation of Stogryn [32] and from local measurements respectively [33]. These liquids were used in the validation of the numerical model. Details regarding the computation of the dielectric data of the system components can be found in the Annex.

### 3.2. Meshing and resolution

To achieve a mesh-independent solution, the distance between the nodes should be enough close so as to minimize interpolation errors. The distance between the nodes in a dielectric is recommended to be less than ($\lambda/5$) with ($\lambda$) being the unguided wavelength of the EM irradiation in the dielectric [34].

Meshing the geometry was done using the built-in mesh generator in the software. Air, quartz and fiber-thickness domains were meshed with the presetting (Fine), Only the solvent domain was tested for different meshes: it is important to well represent the *E*-field on the solvent domain as this directly affects the simulated levels of absorbed powers. Three different mesh configurations were tested herein: Finer, Extra Fine, and Extremely Fine as detailed in Table 3-2.

Table 3-2 shows that the average size for all three meshes satisfies the requirements of good meshing, i.e. the average element size is lower than or equal to one-fifth of the wavelength of the EM irradiation in the solvent domain ($\lambda$ = 1.38 cm for distilled water). It is partly for this reason that the average *E*-field on the solvent domain is independent from the mesh.

**Table 3-1**
complex permittivity of materials used in the EM simulation at f = 2450 MHz.

| | |
|---|---|
| Fused quartz [30] | 3.78 |
| PTFE [30] | 3.15 |
| Porous PTFE | 1.44 |
| Distilled water-20 °C [32] | 78.62- j10.53 |
| 30 wt% ETA-20 °C, α = 0.44[33] | 56.83- j 45.36 |
| 30 wt% ETA-60 °C, α = 0.44[33] | 61.31- j 63.48 |
| 30 wt% ETA-80 °C, α = 0.44[33] | 61.13- j 75.12 |

### 3.3. Results: model validation: distilled water flowing into the fiber

In order to validate the modeling of the electromagnetic phenomenon, simulated and real levels of reflected powers were compared. If both data sets agree, this means that the simulation was able to well-predict the rate of absorbance of MW energy, hence the *E*-field maps inside the lossy material. Comparison was performed by either varying the position of the SSC, or by varying the frequency of the EM irradiation. It should be highlighted that both methods of validation are somewhat equivalent. A vector network analyzer (ENA 5062 A, Agilent Technologies, Malaysia) was connected to the waveguide transition instead of the microwave generator. The VNA is able to generate low power EM waves and to record the norm of reflected *E*-field waves, in order to obtain the ($S_{11}$) spectrum over [2400–2500 MHz]; the SSC was adjusted to place minimal levels of reflected powers at f = 2450 MHz. The ($S_{11}$) parameter is defined in, with ($E_r$) being norm of the reflected E-field wave, ($E_i$) that of the incident wave, while ($\theta$) is the phase difference. We define the optimum SSC position, as that which places the minima of the reflected power spectrum at f = 2450 MHz. The ($S_{11}$) parameter can be represented in (dB) scale as shown in (3–5.

$$S_{11}(dB) = 10\log_{10}[P_r/P_i] \quad (3\text{-}5)$$

The model was validated by comparing the simulated and experimental reflected powers spectra when distilled water (DW) - that acts as absorbents of EM irradiation- circulated in the lumen region of the hollow fiber. The use of distilled water instead of 30 wt% ETA + $CO_2$ was motivated by the very well documented dielectric properties of the former, whereas data on the properties of the latter are practically non-existent. Fig. 3-2 presents both the experimental and computed power reflection spectra: the experimental (VNA) results, the simulated ($P_r$) at the experimental optimum SSC position, as well at the simulated ($P_r$) optimum SSC position. Results show that experimental and simulated curves have similar tendencies, but the simulated curve corresponding to the real position of the SSC is shifted to higher frequencies. This can be explained by many reasons: errors in the estimation of dielectric properties, the geometrical dimensions of the applicator and waveguide, error in calibrating the VNA, as well as other simplifying assumptions. Increasing the SSC position from 103.8 mm (experimental adjustment)

**Table 3-2**
Characteristics of different mesh types on the solvent domain.

| Type | Nodes | Avg. size (mm) | Max size (mm) | Average *E*-field (V/m) |
|---|---|---|---|---|
| Finer | 3067 | 1.324 | 2.11 | 11,571 |
| Extra fine | 10,819 | 0.931 | 1.43 | 11,573 |
| Extremely fine | 28,777 | 0.678 | 1.18 | 11,574 |

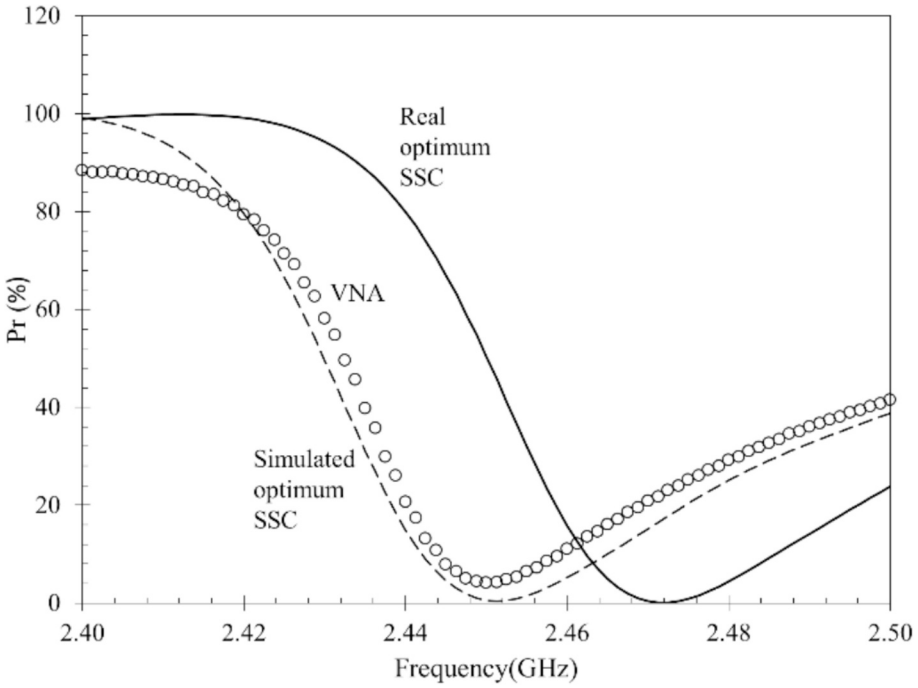



**Fig. 3-2.** Reflected power spectrum with distilled water ($T$ = 20 °C) occupying the lumen region.

to 107 mm places reduces the average relative deviation over [2.4–2.5 GHz] to (~5.5 %).

## 4. Simulation of EM fields: case of 30 wt% ETA enriched with $CO_2$

After experimentally assessing the accuracy of the simulated EM propagation inside the contactor using DW, we attempt to model the system when 30 wt% ETA enriched with $CO_2$ occupies the fiber lumen. This step subscribes to the methodology of progressive complexification of the numerical model, it will be followed by the incorporation of the physical phenomena of heat and momentum transfers.

The *E*-field map was plotted in Fig. 4-1 along the waveguide, and the hollow fiber whose lumen region is occupied with 30 wt% ETA at (α = 0.44) and ($T$ = 60 °C). The incident power at the entry port was chosen arbitrarily, thus Fig. 4-1 serves only as a qualitative representation that is independent from the incident MW power. The planar representation is sufficient given that in the ($TE_{10}$) mode, the *E*-field is invariant with respect to the small dimension (b = 43 mm) of the waveguide. Fig. 4-1 shows that the *E*-field norm is stronger upstream the cavity than downstream. The variations of energy densities between the two regions imply that most of the EM power was absorbed upon first contact with the product. Part of the incident power, which is reflected back to the entry port, resonates with the incident *E*-field; the unabsorbed part of the energy bypasses the solvent and reaches the sliding short circuit where it gets reflected back towards the cavity. To obtain a more quantitative assessment, the *E*-field norm was plotted in Fig. 4-2 along a path (cut-line) that traverses the waveguide for cases where solvent temperature (20, 60, 80 °C) was varied at a constant carbonation ratio (α = 0.44). Fig. 4-2 shows that the different *E*-field curves are "in-phase" upwind of the "product" and displaced from one another towards the SSC, this is due to the different set values of SSC used to reach optimal adaptation. The increased *E*-field norm upwind of the applicator is the consequence of using higher MW entry powers to compensate for the increased power reflection.

Fig. 4-3 presents the *E*-field maps within the solvent domain that fills the lumen side. The figure demonstrates that the *E*-field is constant in the solvent domain inside the MW cavity. This can be attributed to the

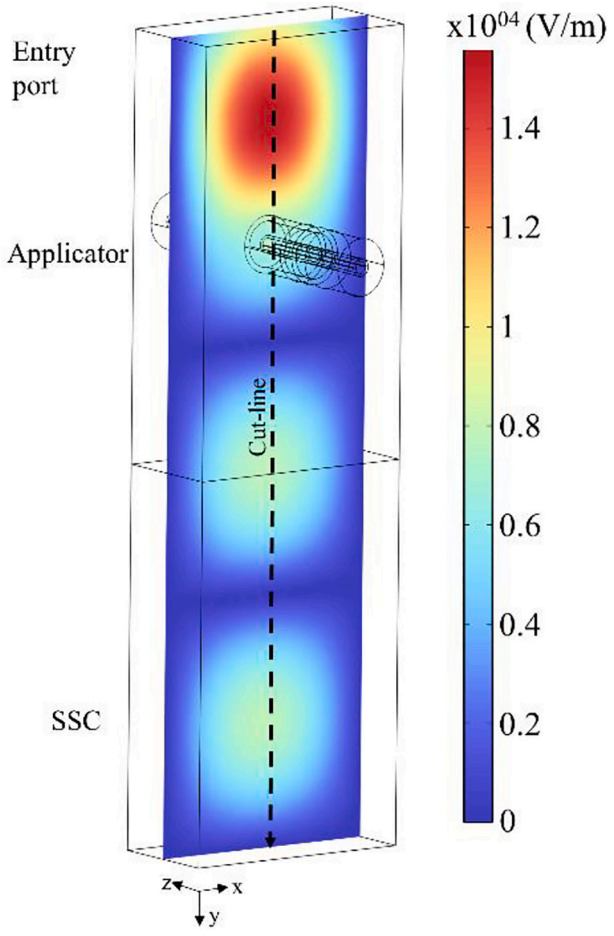



**Fig. 4-1.** *E*-field norm in waveguide (f = 2450 MHz) - case of 30 wt%ETA, α = 0.44, $T$ = 60 °C.

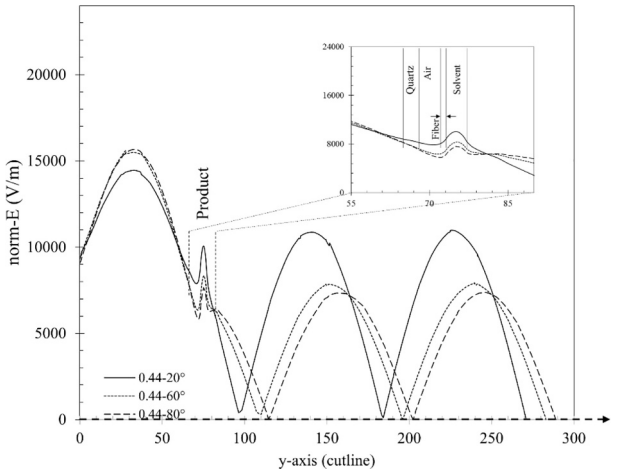



**Fig. 4-2.** Plot of E-field norm on cut-line along the length of the waveguide (f = 2450 MHz). Case 30 wt% ETA (α = 0.44), *T* = 20 °C, 60 °C, 80 °C.

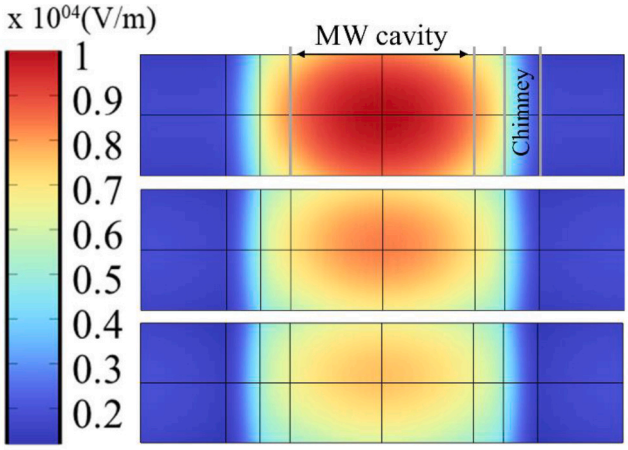



**Fig. 4-3.** E-field in the longitudinal cross-section of the solvent domain at different conditions [T, α]: [20 °C, 0.44], [60 °C, 0.44], [80 °C, 0.44].

lumen radius being considerably lower than the penetration depth of MWs (mention MW penetration depth).

Fig. 4-4 presents the *E*-field maps across the radial cross-section of the fiber at different conditions [T, α]: [20 °C, 0.44], [60 °C, 0.44], and [80 °C, 0.44]. It is interesting to observe that the E-field is more concentrated at the center of the fiber, this results from the superposition of forward and backward traveling EM waves.

### *4.1. Simulating MW heating of solvent flow*

This part capitalizes on the EM simulation previously performed. In this part, the resolution of the energy and momentum balances was incorporated in the model to allow for the simulation of microwave heating of the solvent flowing into the fiber, and the determination of temperature maps. The latter are necessary elements for modeling chemical desorption in non-isothermal conditions.

#### *4.1.1. Energy and momentum conservation equations*

The liquid flow hydrodynamics was described according to the Naviers-Stokes balance equation. The energy balance is expressed in terms of the volumetric dissipation rate of EM energy (Q) in the solvent. The dissipation of heat within the porous membrane, the quartz tube and the gas were assumed non-existent given their negligible loss factor (ε").

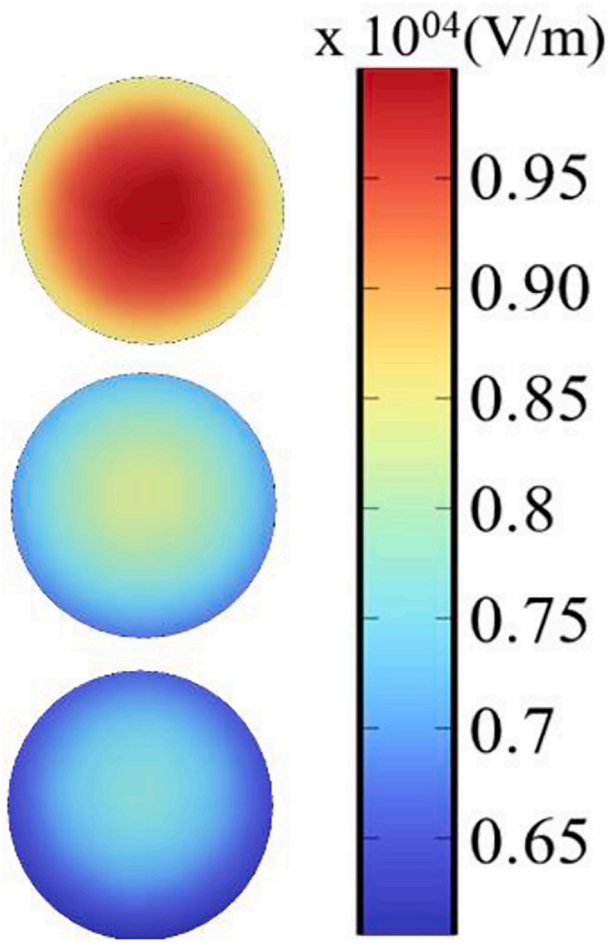



**Fig. 4-4.** E-field in the radial cross-section of the solvent domain at mid-cavity.

$$\text{Naviers} - \text{Stokes Equation} \qquad \rho(\vec{u}.\nabla)\vec{u} = \rho\vec{g} - \nabla P + \mu\nabla^2\vec{u} \tag{4-1}$$

$$\text{Energy Balance} \qquad \rho C_p(\vec{u}.\nabla T) - \nabla.(k\nabla T) = Q \tag{4-2}$$

$$\text{EM dissipation rate} \qquad Q_{W/m^3} = \omega\varepsilon''\varepsilon_0^* E^2 \tag{4-3}$$

In Eq. (4-1), (ρ) is the density of the fluid, (u) is the velocity vector, (g) is the gravitational acceleration, (P) is the pressure, and (μ) is the fluid viscosity. In (4–2, ($C_p$) is the specific heat of the fluid, (T) is the temperature, (k) is the thermal conductivity, and (Q) is the volumetric dissipation rate of EM energy. (Q) is computed according to (4–3 with (ω) being the angular frequency, (ε″) the dielectric loss factor, ($\varepsilon_0^*$) the permittivity of free space and (E) is the RMS-value of the electric field.

Fig. 4-5 illustrates the multi-physical modeling approach under steady state conditions: the temperature of the solvent influences its dielectric properties, while the change in dielectric properties influences the *E*-field maps and hence the volumetric dissipation rate. On the other hand, velocity fields influence convective rate of heat exchange, consequently the change in temperature influences the physical properties of the solvent (ρ, μ).

#### *4.1.2. Boundary conditions*

The boundary conditions of the fluid mechanics and heat-transfer physical phenomena are presented in Table 4-1, while those related to the EM phenomenon are identical to those given in Section 2. ($r_i$) stands for the internal radius of the fiber, (L) its length, ($\vec{n}$) normal vector to the surface, (P) pressure, ($\vec{u}$) the velocity vector of the fluid flow, and ($\vec{q}$) the heat flux.

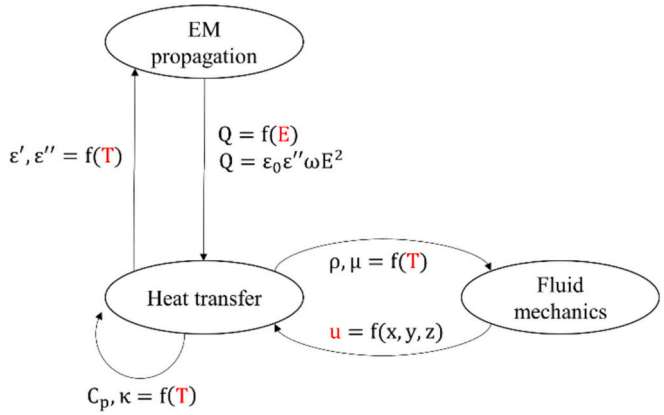



**Fig. 4-5.** Schematic of the equation coupling to model solvent heating by microwave irradiation at steady state.

**Table 4-1**
Boundary conditions for fluid mechanics and heat transfer applied on fiber lumen.

| | Coordinates | Type | Equation |
|---|---|---|---|
| Momentum balance | z = 0 solvent outlet | Constant mass flow | $m_{in} = \int \rho(\vec{u}.\vec{n})dS$ |
| | z = L solvent inlet | Constant pressure condition | $P = 0$ |
| | 0 < z < L; r = $r_i$ radial boundary | Liquid velocity is null at the membrane wall (no-slip condition) | $\vec{u} = 0$ |
| | z = 0 solvent outlet | Heat transfer by conduction is null | $-\vec{n}.\vec{q} = 0$ |
| | z = L solvent inlet | Fixed temperature | $T = T_{in}$ |
| | 0 < z < L; r = $r_i$ radial boundary | Heat transfer between the liquid flow and the membrane was neglected (thermal insulation) | $-\vec{n}.\vec{q} = 0$ |

We assume that under the current operating conditions, the lateral surfaces of the fiber behave as insulator due to the thickness of the PTFE fiber (1 mm) and the low sweeping gas flow rate (3.33–6.66 mL/s) used in experiments (1–8). This was verified numerically where results show that the evacuated thermal power by the $N_2$ gas is in the order of (~0.1 %) with respect to the incident microwave power. The dielectric properties of the solvent were assumed to be invariant with $CO_2$ loading along the length of the fiber as the regeneration rate ($\Delta\alpha = \alpha_{in}$-$\alpha_{out}$) was experimentally found to be very small, hence the dielectric properties only vary due to temperature changes.

### 4.1.3. Resolution and meshing

The coupling between the physical phenomena related to the electromagnetic field, heat transfers was done by the addition of the "Electromagnetic heating" option. Heat transfer and fluid mechanics were coupled by applying the "Non-isothermal Flow" option. The EM phenomenon and fluid mechanics were solved using the (GMRES) solver while energy balance equation was solved using the (PARDISO) algorithm. Resolution of the system is done by a two-step procedure: in step one, the Navier-Stokes equation was exclusively solved to initialize the computation of the velocity field. In step 2, the model solves the whole set of equations taking as initial guess the velocity field calculated in step 1. This procedure was found to reduce the computation time greatly.

With regards to meshing, several configurations were, the setting "Fine" -preset by Comsol®- was used to mesh the entire simulated domain with the exception of the solvent (Fig. 4-6). The latter was meshed in various manners as shown in Table 4-2, either with a predefined Comsol® mesh such: Fine or Extremely Fine. We explored adding several boundary layers (Custom 1 - Custom 2) at ($r = r_i$) to accurately capture the T-gradients in this region. A good compromise between solution time mesh independency could be reached with "Custom 1".

## 4.2. Numerical results

### 4.2.1. MW-heating of distilled water (DW)

In order to validate the numerical model, MW heating experiments using distilled water were performed. Distilled water was made to circulate inside the hollow fiber at different mass flow rates (2–5 mL/s) by steps of 1 mL/s. The MW power incident from the generator was adjusted so as to maintain an outlet temperature from the applicator at 40 °C, whilst the inlet temperature was 20 °C. The incident power from the generator was measured using the six-port reflectometer and was considered as the input power in the model. The use of distilled water was motivated by its well-known physical, dielectric and thermal properties, which is not the case of aqueous ethanolamine solutions, especially when loaded with $CO_2$. The properties of DW are reported in the Annex.

Fig. 4-7 compares the simulated and the experimental outlet temperatures ($T_{out}$) of distilled water at different mass flow rates. Fig. 4-7 shows that the model is able to predict ($T_{out}$) with a very high accuracy for the different tested mass flowrates. Deviations are not completely

**Table 4-2**
Meshing configuration and corresponding averaged quantities over the fiber domain for the case of distilled water.

| Type | Fine | Finer | Extra fine | Extremely fine | Custom 1 | Custom 2 |
|---|---|---|---|---|---|---|
| Number of vertices | 457 | 3176 | 10,828 | 28,836 | 8684 | 35,828 |
| Maximum size (mm) | 3.77 | 2.11 | 1.47 | 1.13 | 2.48 | 1.37 |
| Number of boundary layers | – | – | – | – | 3 | 5 |




**Fig. 4-6.** Meshing of the fiber lumen domain using two different configurations: (a)-Extremely Fine; (b)-Custom 2.

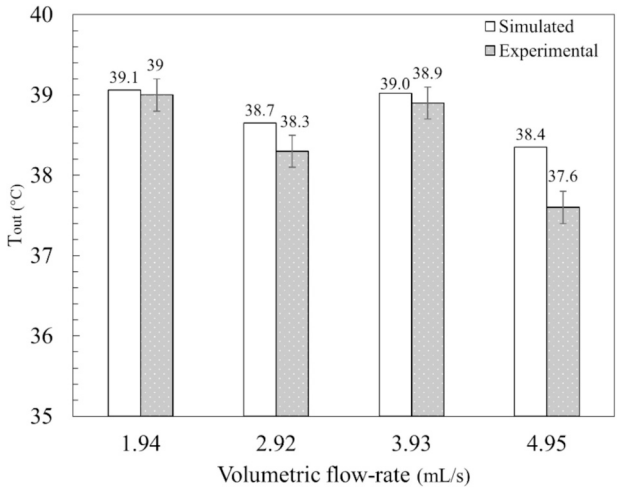



**Fig. 4-7.** Comparison of simulated and experimental outlet temperatures of MW heating of distilled water.

accounted for the uncertitude of measured $T_{out}$ (±0.2 °C), as errors may also derive from the pump (±0.03 mL/s), or even the measurments of absorbed MW power estimated in the range of (± 3 W).

#### 4.2.2. *MW-heating of 30 wt% ETA enriched with $CO_2$*

MW heating of $CO_2$ loaded 30 wt% ETA solutions was simulated at the operating conditions of experiments (1–8) of the experimental design: volumetric flow rate of solvent at 0.2 and 0.6 mL/s, ($T_{out}$) at 50 and 60 °C, solvent carbonation ratio was fixed at ($\alpha = 0.44$). As the lateral surfaces of the fiber were assumed to be adiabatic, the sweeping gas flow rate holds no effect on the temperature maps, hence it is only necessary to simulate experiments (1–4), to the exemption of (5–8). As a reminder, the operating conditions of the experimental design are included in Table 4-3. It is important to highlight that the endothermic nature of the desorption reaction was neglected: the highest experimental regeneration rate obtained by a single pass of the solvent across the MW applicator was ($\Delta\alpha/\alpha_{in}$=0.15 %) due to the very low fiber exchange area. It follows that endothermal effect induced by the desorption reaction accounts to 0.12 % of the microwave power absorbed, and was thus assumed negligible in the operating tested conditions.

In Fig. 4-8, temperature maps are shown over the solvent flow region along the longitudinal section, for the experiments (1–4). Local axial and radial temperature variations are observed, with hotspots located close to the membrane wall in the region of exit flow, thus the region near the liquid entry is deemed "cold" with respect to that near the liquid exit. The magnitude of the local temperature variations is clearly related with the solvent flowrate: the larger the liquid flowrate, the higher the local temperature rises close to the membrane walls at the same mean outlet temperature.

To explain the occurrence of local high temperature rises close to the membrane wall, the velocity field and the *E*-field of experiment (4) were plotted in Fig. 4-9 and 4-10 respectively. The velocity field displays a typical parabolic profile and having its maxima at the fiber center and its minima at the fiber boundary. While the flow stagnates at the boundary of the fiber lumen (stagnant film region), the E-field does not experience radical changes between its center and boundary hence the EM dissipation rate appears uniform over the fiber cross section. Thus, the energy absorbed at the fiber center is easily evacuated due to large local solvent flow velocities, whereas the film region has less convective evacuation of heat which leads to higher temperature levels. As a general rule, it can be said that the use of higher MW powers leads to the accumulation of thermal energy at the fiber boundaries and thus an increase of local temperatures.

The radial and tangential temperature profiles were plotted in Fig. 4-11 and 4-12 respectively, the temperatures were plotted on the paths shown in Fig. 4-13. Fig. 4-11 shows that at the fiber boundaries, the temperature reaches high values then drops swiftly as we move further towards the bulk. In experiments 3 and 4, corresponding to the highest solvent flowrate, the bulk flow is characterized by a temperature plateau. Fig. 4-12 presents the tangential T-profiles to show the heating homogeneity due to the uniform dissipation of MW power.

**Table 4-3**
Operating conditions at experiments (1–8) of the experimental design.

| Experiment | α | $v_{g(mL/s)}$ | $v_{l(mL/s)}$ | $T_{out(°C)}$ |
|---|---|---|---|---|
| 1 | 0.44 | 3.33 | 0.2 | 50 |
| 2 | 0.44 | 3.33 | 0.2 | 60 |
| 3 | 0.44 | 3.33 | 0.6 | 50 |
| 4 | 0.44 | 3.33 | 0.6 | 60 |
| 5 | 0.44 | 6.66 | 0.2 | 50 |
| 6 | 0.44 | 6.66 | 0.2 | 60 |
| 7 | 0.44 | 6.66 | 0.6 | 50 |
| 8 | 0.44 | 6.66 | 0.6 | 60 |

## 5. Desorption process modeling across the hollow fiber

This part focuses on the theoretical description of mass-transfer combined with chemical desorption reaction described by the resistance-in-series model. First, a theoretical background regarding reactive mass-transfer phenomena are laid-out, for conditions of wetting and non-wetting of the membrane material. The model simulating the desorption process at isothermal condition was first established and validated with experimental data from the literature. This model was afterwards extended to describe the chemical desorption process assuming axial and radial temperature variations in the solvent.

### 5.1. *Resistance in series for modeling mass-transfer*

In a membrane process, mass-transfer takes place between the liquid and the gas bulks. Over an elementary volume of the fiber, three transport resistances are accounted for, as shown in Fig. 5-1:

1. The liquid film adjacent to the internal membrane surface is stagnant, therefore a concentration gradient is formed implying a resistance to molecular diffusion.
2. Porous membrane: The stagnant gas filling the pores, as well as the tortuosity of the traveled path poses a resistance to mass-transfer. Equal pressures on both sides of the membrane dictate that diffusive transfer takes place via the molecular and the Knudsen diffusions.
3. Gas film: The thin film in contact with the outer surface of the membrane induces a supplementary mass transfer resistance.

The resistance-in-series model is useful in order to calculate the overall mass transfer coefficient across all three resisting phases, starting from partial mass transfer coefficients in the liquid, membrane, and gas films, which are presented in Eqs. (5-1), (5-2), and (5-3) respectively. In these equations the subscripts (l), (m), and (g) stand for liquid, membrane and gas respectively while subscript (i) stands for interface, (N) is the solute transfer rate, (A) is the surface area of gas-liquid contact, (k) is the partial mass transfer coefficient, and (C) is the concentration of physically dissolved volatile species.

$$N_l = A_l k_l \left(C_l - C_{l-m,i}\right) \tag{5-1}$$

$$N_m = A_m k_m \left(P_{l-m,i} - P_{m-g,i}\right) \tag{5-2}$$

$$N_g = A_g k_g \left(P_{m-g,i} - P_g\right) \tag{5-3}$$

Rearranging and using the partition coefficient ($He_c = P/C^*$), Eqs.

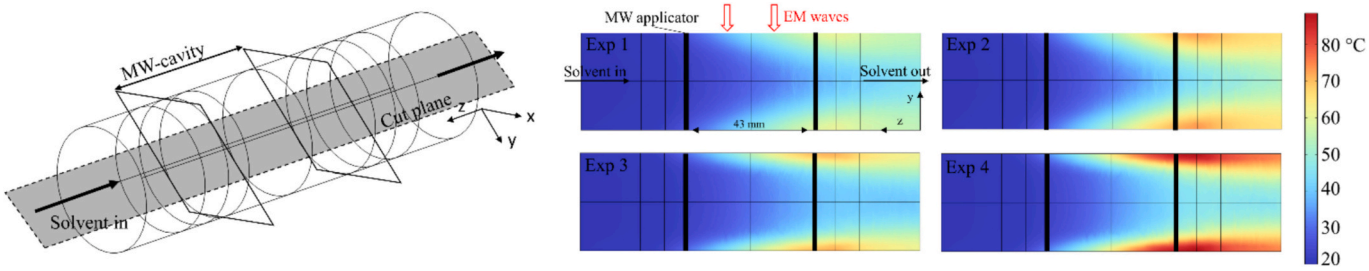



**Fig. 4-8.** Simulated temperature maps on the longitudinal (ZY) cross-section of the hollow fiber for different experiments [$v_l$, $T_{out}$]: Exp 1 - [0.2, 50]; Exp 2 - [0.2, 60]; Exp 3 – [0.6, 50]; Exp 4- [0.6, 60].

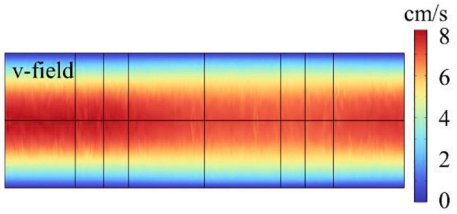



**Fig. 4-9.** Velocity map in fiber lumen at operating conditions of Exp 4: $v_l = 0.6$ mL/s, $T_{out} = 60$ °C, $\alpha = 0.44$.

(5-1) to (5-3) become (5–4) with the superscript (*) designating the hypothetical concentration of a liquid phase at equilibrium with the partial pressure of the solute (or volatile component) in the gas bulk at the shell side.

$$N = \frac{C_l - C_g^*}{\frac{1}{A_i k_l} + \frac{1}{A_m k_m He_c} + \frac{1}{A_g k_g He_c}} \tag{5-4}$$

The mass-transfer rate is expressed in (5–5) with respect to the driving force for mass transfer, the surface area of exchange ($A_l$) of the fiber lumen, and the over-all mass-transfer coefficient ($K_L$) as expressed in (5–6).

$$N = \left(C_l - C_g^*\right) K_L A_l \tag{5-5}$$

$$\frac{1}{K_L} = \frac{1}{k_l} + \frac{d_i}{d_{ln} k_m He_c} + \frac{d_i}{d_o k_g He_c} \tag{5-6}$$

*5.1.1. Liquid phase mass-transfer coefficient*

The liquid phase mass transfer correlation ($k_l$) first derived by Graetz [35] is expressed in Eq. (5-7) with ($d_i$) and (l) being the diameter and the length of the fiber, (*Sh*) the Sherwood number, (*Re*) the Reynold's number, and (*Sc*) being the Schmidt number. The expressions of the dimensionless numbers are given in (5–8), with ($D_l$) being the diffusivity of the solute in the liquid phase, (u) the average velocity of the solvent in the fiber lumen, (μ) the solvent viscosity.

$$Sh = 1,615\left(Re.Sc.\frac{d_i}{l}\right)^{\frac{1}{3}} \tag{5-7}$$

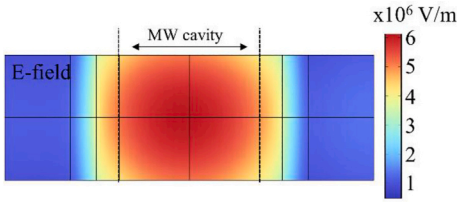



**Fig. 4-10.** Electric field map in fiber lumen at operating conditions of Exp 4: $v_l = 0.6$ mL/s, $T_{out} = 60$ °C, $\alpha = 0.44$.

$$Sh = \frac{k_l d_i}{D_l} \Big/\Big/ Re = \frac{\rho\, d_i\, u}{\mu} \Big/\Big/ Sc = \frac{\mu}{\rho\, D_l} \tag{5-8}$$

The expression of the physical mass-transfer coefficient in the hollow fiber lumen in (5–9). The expression of the diffusivity of $CO_2$ in carbonated 30 wt% ETA can be found in the Annex.

$$k_l = 1,615\left(\frac{u}{l}.\frac{D_l^2}{d_i}\right)^{\frac{1}{3}} \tag{5-9}$$

*5.1.2. Membrane mass-transfer coefficient*

The resistance to mass-transfer in the membrane depends on the operating conditions, such that high operating trans-membrane pressure may lead to the intrusion of the liquid phase into the pores [36]. The membrane wetting is known to have adverse effects on mass-transfer performance, as the diffusivity of the solute in the wetted pores is a few orders of magnitude lower than in gas-filled ones. We note that other wetting mechanisms can occur such as condensation wetting which may take place when the solute vapors cool down and condenses inside the membrane pores. The membrane mass-transfer coefficient is estimated considering either non-wetting or partially wetted modes.

Non-wetted mode.

In the non-wetted mode, the mass transfer coefficient – ($k_m$) (m/s) - is calculated from (5–10) [37]. (τ) being the tortuosity and expressed in (5–11) and obtained from [38,39], ($D_{g,eff}$) is the solute effective diffusivity in the pores filled with the gas phase ($m^2$/s), (δ) being the membrane thickness (m), and (ξ) is the connected porosity of the membrane.

$$k_M = \left[D_{g,eff}\, \xi\right] / \left[\tau\, \delta\right] \tag{5-10}$$

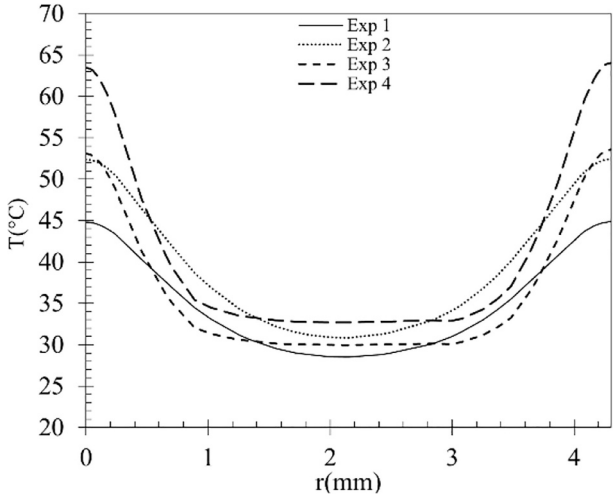



**Fig. 4-11.** Radial temperature profiles at "mid-cavity" position for experiments (1–4).

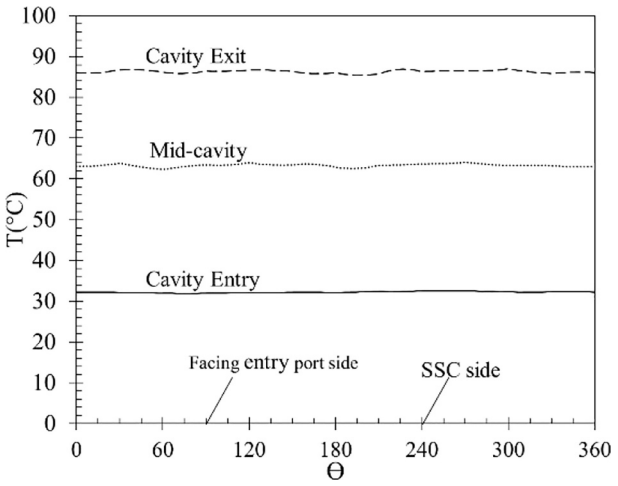



**Fig. 4-12.** Tangential temperature profiles at $r = r_i$ and for $0 < \Theta < 360°$ at operating conditions of experiment 4 [0.6 mL/s, $T_{out} = 60$ °C].

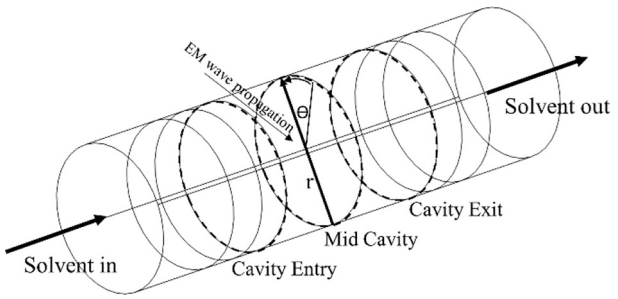



**Fig. 4-13.** Schematic showing the paths over which temperature was evaluated.

$$\tau = 1/\xi^2 \tag{5-11}$$

When the solute diffuses through the membrane pores it encounters resistances originating from collisions with gas molecules (molecular diffusion), and collisions with the pore walls (Knudsen diffusion). The effective diffusivity ($D_{g,eff}$) is calculated as per (5–12) [40–42], with ($D_g$) accounting for the molecular diffusion of the solute in the gas phase, while ($D_{kn}$) accounts for the Knudsen diffusion.

$$\frac{1}{D_{g,eff}} = \frac{1}{D_g} + \frac{1}{D_{kn}} \tag{5-12}$$

The molecular diffusivity of $CO_2$ is given in the appendix, while the Knudsen diffusivity is expressed according to Eq. (5-13) with r being the mean pore size in (cm), M the molar mass of $CO_2$ (g/mol), and R the ideal gas constant (J/mol. K).

$$D_{kn} = \frac{2}{3} r \sqrt{[8RT/\pi M_{CO_2}]} \tag{5-13}$$

Partially wetted mode.

When the membrane pores are partially wetted, the membrane mass transfer coefficient is greatly reduced, as observed by many authors [17,39,43–46]. Reduction in mass transfer rates resulting from the diffusivity of the liquid filling the pores is about a few orders of magnitude higher compared when no wetting takes place. The physical mass transfer coefficient in partially wetted membrane pores is expressed according to Eq. (5-14) [44,45,47] with (F) being the wetted fraction of the pores thickness as represented in Fig. 5-2, ($D_{g,eff}$) the effective diffusivity of the solute in the gas filling the pores of the membrane, ($D_l$) the diffusivity of the solute in the liquid phase, and ($He_c$) is the gas-liquid partition coefficient.

$$\frac{1}{k_m} = \frac{\delta\tau(1-F)}{D_{g,eff}\,\xi} + \frac{\delta\tau(F)He_c}{D_l\,\xi} \tag{5-14}$$

The first term of (5–14) accounts for resistance in the non-wetted region of the membrane, while the second accounts for that in the wetted region of the membrane.

Effect of chemical reaction on liquid phase mass-transfer coefficient.

Chemical desorption involves the release of chemically bound $CO_2$ by the dissociation of carbamate ion ($ETACOO^-$) to produce $CO_2$ and ETA molecules as per reaction (5-15).

$$ETACOO^- + ETAH^+ \Longleftrightarrow 2\,ETA + CO_2 \tag{5-15}$$

There exists different levels of complexity in modeling chemical absorption of $CO_2$, it can be as tedious as kinetic modeling with the whole set of chemical reactions being assigned forward and reverse reaction rates, and it can be as convenient as assuming the absorption reaction to be irreversible as implied by the pseudo-first order assumption [48]. Within the framework of the resistance-in-series model, it is possible to account for the effect of the chemical acceleration of the desorption through the inclusion of an enhancement factor (E) as introduced in Eq. (5-16).

$$\frac{1}{K_L} = \frac{1}{E_{rxn}k_l} + \frac{d_i}{d_{ln}k_m\,He_c} \tag{5-16}$$

Therefore, the desorption rate results from two contributions: the

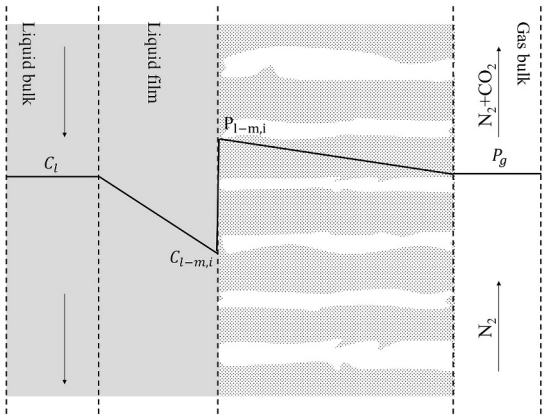



**Fig. 5-1.** Schematic of the resistance in series model for mass-transfer, gas filled membrane.

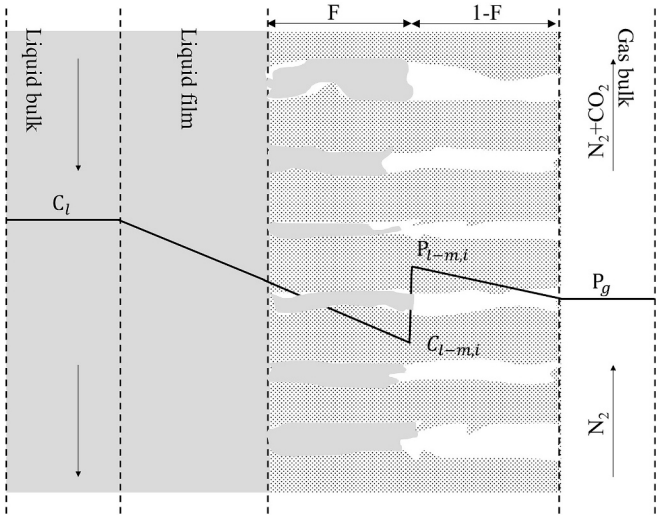



**Fig. 5-2.** Schematic of the resistance in series model for mass-transfer, partially wetted mode of operation.

diffusion of $CO_2$ from the liquid bulk to the gas bulk, or the generation of $CO_2$ in the liquid film by dissociation of carbamate ion at increasing temperature. In our work we chose the expression of the enhancement factor as derived by Astarita [49] and used by others [18,39,41,50]. The analytical derivation of the enhancement factor is based on the assumptions:

- o A single reaction describes the absorption of $CO_2$ (2ETA + CO2↔ETACOO- + ETAH+)
- o The reaction is infinitely fast, i.e. chemical equilibrium is instantaneous
- o Applicability of physical equilibrium at liquid-gas interface (Henry's law)
- o Transfer by molecular diffusion in both the liquid and gas films

The expression of the enhancement factor is given in (5–17), where ($D_p$) is the diffusivity of the carbamate ion, ($D_{co_2}$) is the diffusivity of $CO_2$ in the solvent phase, ($C_{ETA}$) is the concentration of free unreacted ethanolamine in the liquid bulk (mol/m$^3$) expressed in (5–18), ($D_{ETA}$) is the diffusivity of ethanolamine in the aqueous solvent, ($c_t$) is the total concentration of the solvent components (mol/m$^3$), ($x^*_{f,i}$) is the mole fraction of free unreacted $CO_2$ at the liquid-membrane interface (i), ($x_{f,l}$) is the mole fraction of free unreacted $CO_2$ in the liquid bulk (l). Free $CO_2$ is dissolved in its molecular form in the liquid bulk phase and is represented by the subscript (f), this comes contrary to the chemically dissolved $CO_2$ that is under the form of carbamate ions.

$$E_{rxn} = 1 + \frac{\frac{D_p}{D_{CO_2}}\sqrt{K}C_{ETA}}{\left[1 + 2\frac{D_p}{D_{ETA}}\sqrt{K\left(c_t x^*_{f,i}\right)}\right]\left[\sqrt{c_t x_{fj,l}} + \sqrt{c_t x^*_{f,i}}\right]} \quad (5\text{-}17)$$

$$C_{ETA,f} = C_{ETA,0}(1 - 2\alpha) \quad (5\text{-}18)$$

The equilibrium constant of the reaction (K) is presented in (5–19) with respect to the absorption reaction of $CO_2$ in ETA, with (α) being the carbonation ratio and ($C_{CO_2,f,l}$) being the free $CO_2$ concentration in the liquid bulk.

$$K = \frac{[\alpha C_{ETA0}]^2}{C_{CO_2,f,l}\cdot[(1-2\alpha)C_{ETA0}]^2} = \frac{1}{C_{CO_2,f,l}}\left[\frac{\alpha}{1-2\alpha}\right]^2 \quad (5\text{-}19)$$

### 5.2. Model equations and implementation

The $CO_2$ desorption process along the hollow fiber is represented in Fig. 5-3, where the solvent circulates in the lumen side and the sweeping gas in the shell side in a counter-current manner. The overall mass balances derived for the fiber are similar to the ones of a classical packed column: at (z = 0) marks the section of sweeping-gas entry, and (z = L) – the section of solvent entry. The nomenclature of the different streams throughout the cross section of an elementary volume are presented in Fig. 5-4. To model the chemical desorption rates of $CO_2$ along the hollow fiber, the set of differential mass balance was solved to predict the average $CO_2$ flux across the hollow fiber ($J_{CO_2}$). The numerical model consists of solving a set of 4 main equations on each differential element of the fiber to produce a solution vector $\left[x, x_{f,l}, x^*_{f,i}, y\right] = f(z)$. It should be noted that water evaporation was neglected, as the condensate collected from the gas phase during the experimental tests proved to be negligible after several hours of operation.

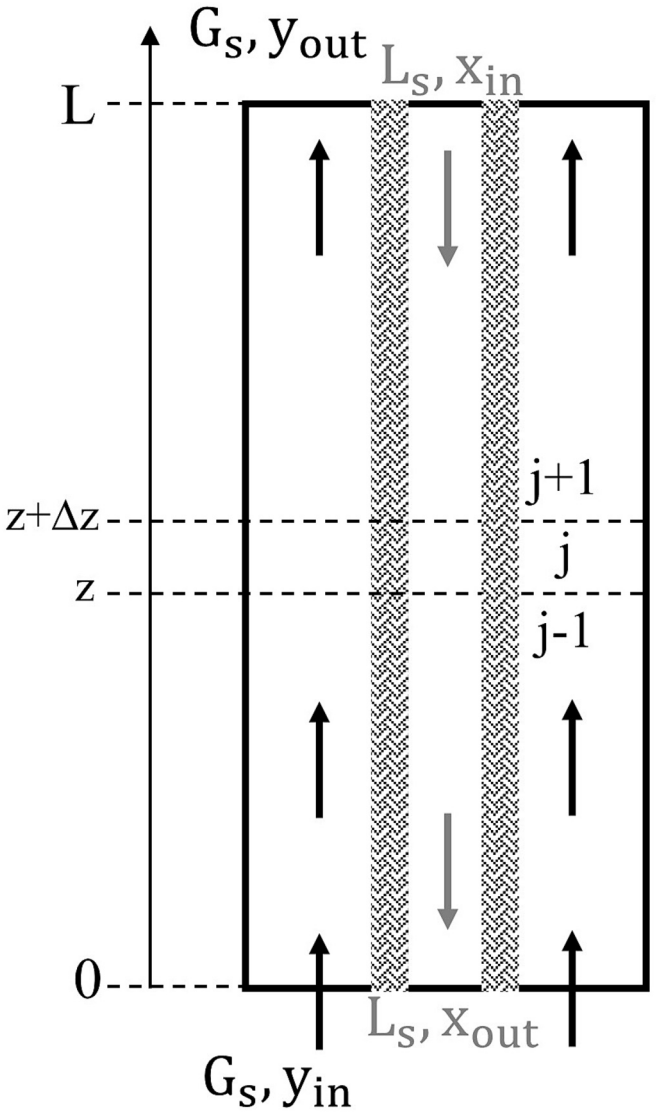



**Fig. 5-3.** Schematic of chemical desorption across a single hollow fiber.

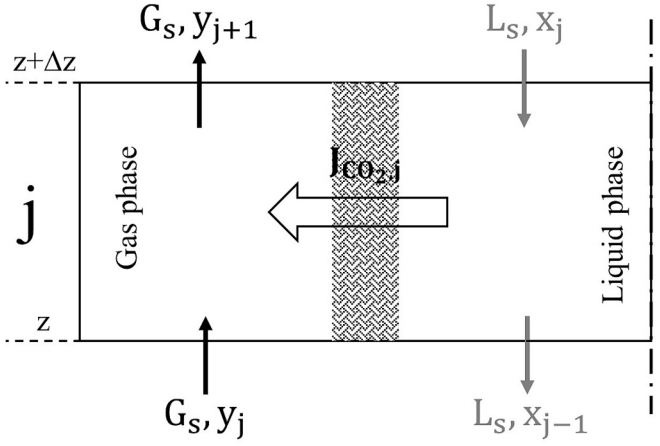



**Fig. 5-4.** Differential mass balance.

#### 5.2.1. Model equations

Operating curve.

The operating curve is a mass-balance between the bottom section of the fiber (z = 0) and that at a given height (z). The equation of the operating line is presented in (5–20), with ($L_s$) and ($G_s$) are the molar flow rates (mol/s) of the inert components in the liquid phase and the gas phase respectively. This expression relates the mole fractions of $CO_2$ in both phases with the inert flow rates of liquid and gas phases. The advantage of such a formulation is that variations of total molar flow rates are accounted for so that the non-linearity of the operating curve

can when necessary be considered.

$$y = \left[\frac{y_{in}}{1-y_{in}} + \frac{L_s}{G_s}\left(\frac{x}{1-x} - \frac{x_{out}}{1-x_{out}}\right)\right] \Big/ \left[1 + \frac{y_{in}}{1-y_{in}} + \frac{L_s}{G_s}\left(\frac{x}{1-x} - \frac{x_{out}}{1-x_{out}}\right)\right] \quad (5\text{-}20)$$

Differential mass balance.

The general form of the differential mass-balance equation is presented in (5–21), with ($K_L$) being the overall mass-transfer coefficient (m/s) with respect to the liquid-phase, (a) the surface density of exchange at the fiber interior per unit length ($m^2$/ m), ($c_{f,l}$) is the free concentration of the ($CO_2$) in the liquid bulk (mol/$m^3$), ($c_g^*$) is the concentration of free $CO_2$ in a hypothetical liquid phase at equilibrium with the gas bulk (mol/ $m^3$), and X is the molar ratio of total dissolved $CO_2$ with respect inert species.

$$L_s \frac{dX}{dz} = K_L\, a \left(c_{f,l} - c_g^*\right) \quad (5\text{-}21)$$

The free concentration of $CO_2$ in the liquid bulk can be presented in terms of its mole fraction ($x_{f,l}$), and the total concentration in the liquid ($c_t$) as given by (5–22). The total concentration was obtained from Eq. (5-23) with ($\rho$) being the density of 30 wt% ETA loaded with $CO_2$, and $\overline{MW}$ its average molecular weight.

$$c_{f,l} = c_t x_{f,l} \quad (5\text{-}22)$$

$$c_t = \rho(T, \alpha)/\overline{MW} \quad (5\text{-}23)$$

The concentration of free $CO_2$, in the solvent phase supposed in equilibrium with the gas bulk, can be obtained by applying Henry's law as shown in (5–24) with (He) being the solubility of $CO_2$ in 30 wt% ETA at ambient pressure.

$$c_g^* = y \Big/ He \quad (5\text{-}24)$$

Replacing (5–22) and (5–24) in (5–21) and substituting the ($X = x/1 - x$) we get a modified expression of the differential mass balance given in (5–25).

$$\frac{L_s}{(1-x)^2}\frac{dx}{dz} = K_L\, a\, c_t \left(x_{f,l} - \frac{y}{He\, c_t}\right) \quad (5\text{-}25)$$

Vapor-liquid equilibrium.

The dissolved $CO_2$ in the solvent is either chemically bound under the form of carbamate ions ($ETACOO^-$), or exists in its molecular form (physically dissolved). While the concentration of chemically bound carbon in the liquid bulk can be easily derived from the carbonation ratio ($\alpha$), that of free carbon – although much less considerable- is less straightforward to determine. By using a VLE model, it is possible to plot

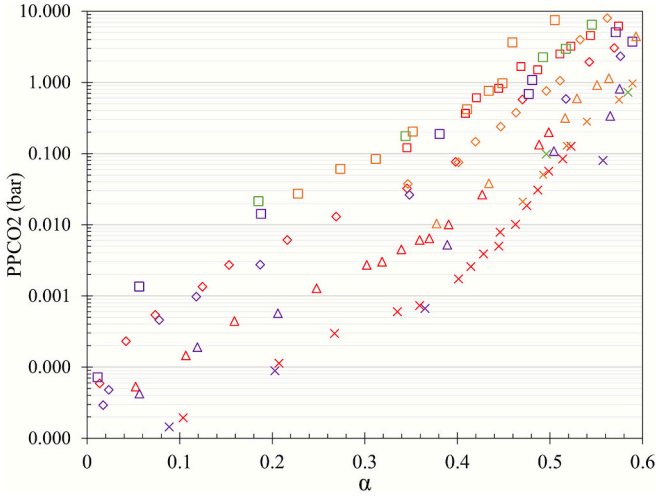



**Fig. 5-5.** Vapor-liquid equilibrium plot of $CO_2$ with 30 wt% ETA as a function of the carbonation ratio at different temperatures: (x)-40 °C, (Δ)-60 °C, (□)-80 °C; (◇)-100 °C. Colors indicate the source of each data set: Red- [55], Violet- [54], orange- [56], green- [57]. (For interpretation of the references to colour in this figure legend, the reader is referred to the web version of this article.)

e. by using relation. The mole fraction ($x_{f,l}$) can then easily be computed and introduced in the differential mass-balance. Several correlations for vapor-liquid equilibrium for $H_2O$-ETA-$CO_2$ are proposed in literature such as those given by Weiland [50] or by Koonaphapdeelert [18]. For greater accuracy, we preferred to describe chemical equilibrium from real experimental data extracted from literature. Fig. 5-5 presents a compilation of experimental equilibrium data for 30 wt% ETA as a function of carbonation ratio and temperature.

$$y = f(\alpha, T) \quad (5\text{-}26)$$

Flux Continuity.

The calculation of the enhancement factor – accounting for the effect of chemical reaction on mass transfer - necessitates the knowledge of the mole fraction of free unreacted $CO_2$ at the membrane-liquid interface, $x_{f,i}^*$. This value can be calculated by equating $CO_2$ desorption rates between the liquid phase and the gas phase in permanent regime which produces (5–27): ($a_l$) represents the mass-transfer at the internal diameter of the fiber, and ($a_m$) being the mass-transfer area computed from the logarithmic mean diameter of fiber thickness.

$$a_l k_l \left[1 + \frac{(D_p/D_{CO_2})\sqrt{K}\, C_{ETA}}{\left[1 + 2(D_p/D_{am})\sqrt{K\left(c_t x_{f,i}^*\right)}\right]\left[\sqrt{c_t x_{f,l}} + \sqrt{c_t x_{f,i}^*}\right]}\right] c_t\left(x_{f,l} - x_{f,i}^*\right) - a_m k_m \left(c_t\, He\, x_{f,i}^* - y\right) = 0 \quad (5\text{-}27)$$

the chemical speciation with respect to operating conditions, the free $CO_2$ included. This method however is not preferred as VLE data have low accuracy as reported in [51–54]; it is for this reason that the free concentration is determined in another manner. Starting from the carbonation ratio and temperature, the mole fraction of $CO_2$ in a hypothetical gas phase in equilibrium with the solvent bulk can be calculated using chemical equilibrium relation in (5–26). The obtained mole fraction of $CO_2$ in the gas phase is then used in conjunction with Henry's law to find the concentration of free molecular $CO_2$ in the liquid phase, i.

### 5.3. *Model validation: chemical desorption in a hollow fiber at isothermal conditions*

Before attempting to model MW-assisted chemical desorption, the modeling of mass-transfer phenomena with chemical reaction is to be validated independently from other phenomena. For this reason, chemical desorption was simulated to replicate the experiments of Koonaphapdeelert [18]. The author performed $CO_2$ desorption with $N_2$ gas sweeping from 15 %wt. ETA solution using a module composed of

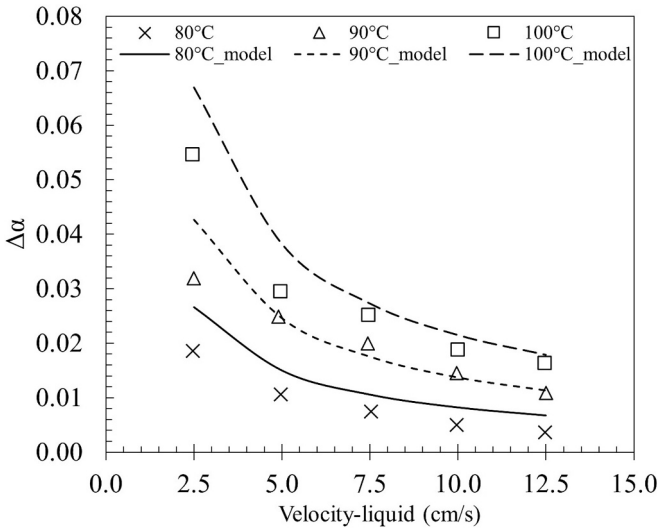



**Fig. 5-6.** Isothermal regeneration of 15 %wt. ETA at varying temperatures and liquid velocities: comparing the simulated results to experimental data of [18]. (Lines)- predictions from numerical model; (symbols)- experimental data.

surface modified ceramic hollow fibers, maintained in isothermal conditions. Fig. 5-6 shows the experimental and simulated regeneration extent ($\Delta\alpha = \alpha_{in}$-$\alpha_{out}$) of 15 %wt. ETA solution as a function of liquid velocity at different temperatures. Fig. 5-6 shows the good agreement between both sets of data which accords confidence in the mass transfer model. This validates the correctness of its underlying assumptions, its implementation, and input data such as correlations of physical and transfer properties. It is worthy to note that observed discrepancies may arise from several reasons, on the part of the author this includes:

- o Deviation from isothermal conditions
- o Inaccurate measurement of $CO_2$ loading
- o Occurrence of membrane wetting

On the part of the numerical model errors may arise from:

- o Inaccurate estimation of transfer properties
- o Assumption of infinitely fast chemical reaction

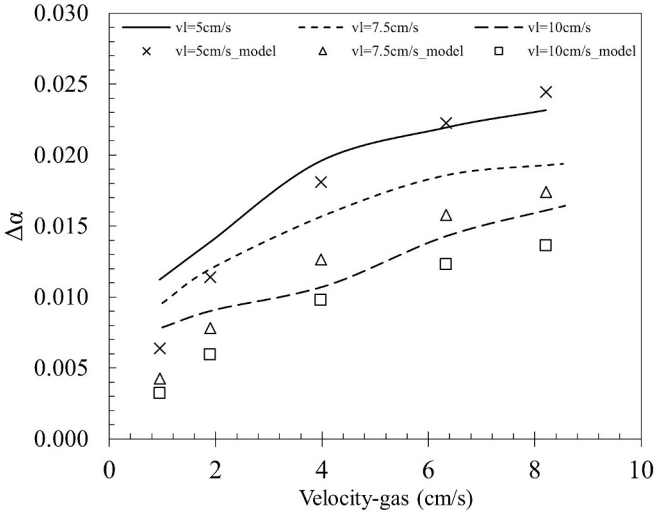



**Fig. 5-7.** Isothermal regeneration of 15 %wt. ETA at varying liquid and gas velocities: comparing the simulated results to experimental data of [18]. (Lines)- predictions from numerical model; (symbols)- experimental data.

Fig. 5-7 presents the experimental and predicted regeneration rates as a function of gas velocity at different liquid flow rates. The figure shows a general agreement between both sets of data with higher deviations at low gas velocities; this is due to the contribution of the mass-transfer resistance in the gas phase which the model does not account for.

## 6. Coupling MW solvent flow heating with chemical $CO_2$ desorption

Till now, chemical desorption was modeled using the 1D resistance-in-series model while the MW-heating model is 3D. The modeling of chemical desorption necessitates the coupling of both models, albeit this requires downscaling the 3D temperature maps to a single dimension to ensure compatibility with desorption model.

### 6.1. Downscaling 3D T-maps to 1D profiles

The 3D T-maps were reduced to two 1D profiles: one for the liquid film region, and for the bulk region. The film region is that occupied by the stagnant liquid film defined arbitrarily by the criteria ($u < 5\ \%\ u_{max}$), the bulk region is the core of the cross-section as described in Fig. 6-1. The temperature over each region of the cross section was averaged to obtain two 1D axial profiles. It is noteworthy to say that in this work we presented a first approach in obtaining 1D T-profiles from 3D maps; the choice of the film and bulk regions of the fiber was made in an intuitive manner. It remains important to establish some physical reasoning that well demarks the film and the bulk regions.

The derived "bulk" and "film" temperature axial profiles are plotted in Fig. 6-2 and 6-3 respectively, for experiments (1–4) of the experimental design. Fig. 6-2 shows that the bulk temperature profile has a linear increase from ($T_{in} = 20\ °C$) at the cavity entrance till ($T_{out}$) at the exit, irrespective of the solvent mass flow-rate due to uniform EM power loss density as mentioned earlier. In Fig. 6-3, the film temperature increases before the liquid exit region are significant compared to ($T_{out}$).

The axial temperature profiles were fitted with a polynomial of the fifth degree – i.e. ($T = f(z)$), and integrated into the non-isothermal mass transfer model such that each position along the hollow fiber has a unique temperature couple [$T_{bulk}(z)$, $T_{film}(z)$]. Consequently, all physical, transfer and chemical properties of the system are evaluated as function of temperature in each region of the liquid flow to compute variations of local desorption flux along the fiber. The coupling between MW-heating and chemical desorption is presented in Fig. 6-4.

One important detail is to determine based on which temperature profile should a quantity be evaluated. Table 6-1 elaborates the choice of temperatures used to evaluated the chemical and transfer quantities of the model - the T-dependent quantities used to calculate the mass transfer coefficients ($k_l$, $k_m$, E, $K_L$) or the driving force ($x^*_{f,i} - y/(c_t\ He)$).

### 6.2. Resolution and boundary conditions

The current fiber of length of 113 mm was uniformly divided into 400 elements. Over each element, the system of equations were solved using finite difference method to produce the solution vector [$x, x_{f,l}, x^*_{f,i}$, $y$] = $f(z)$. The equations were implemented in a Matlab® code. Model inputs are membrane properties, inlet solvent composition, as well as the operating conditions which include gas and liquid volumetric flow rates ($u_g$) and ($u_l$) respectively, in addition to bulk ($T_{bulk}$) and film ($T_{film}$) axial temperature corresponding to the tested conditions in experiments (1–4). The model is starts at one end ($z = 0$) and moves towards the other ($z = L$). Initially, only the compositions of inlet gas and liquid streams are known ($x_{in}$, $y_{in}$) therefore, in a counter-current operation, it is necessary to guess the boundary conditions ($x_{out}$,$y_{out}$). At the end of the resolution, $CO_2$-balance on the fiber is used to test proximity of ($y_{out}$) calculated to the guessed one ($y_{out,g}$). For a co-current mode of

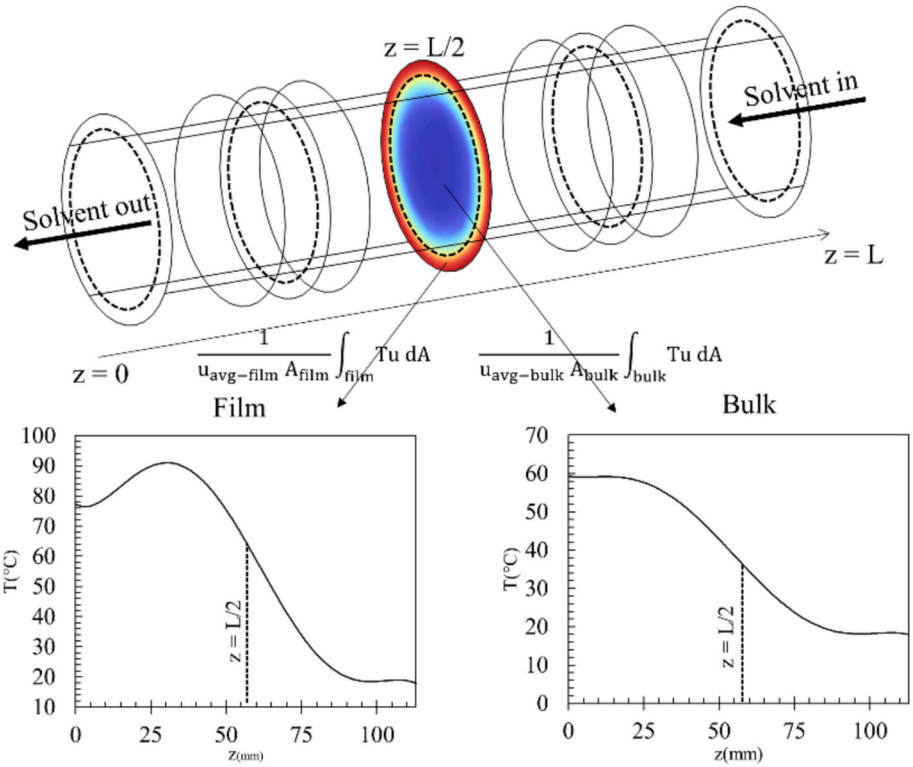



**Fig. 6-1.** Transformation of a 3D T-maps into bulk and film T-profiles.

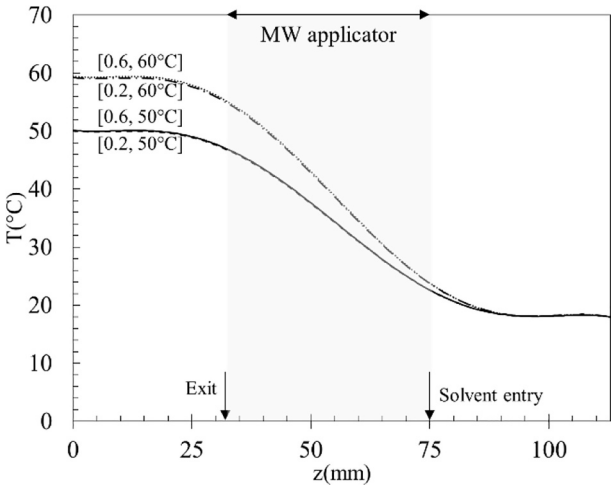



**Fig. 6-2.** Longitudinal temperature profiles of the bulk region at operating conditions [mass flow-rate, $T_{out}$] of experiments (1–4): Exp(1)-[0.2, 50]; Exp (2)-[0.6, 50]; Exp(3)-[0.2, 60]; Exp(4)-[0.6, 60].

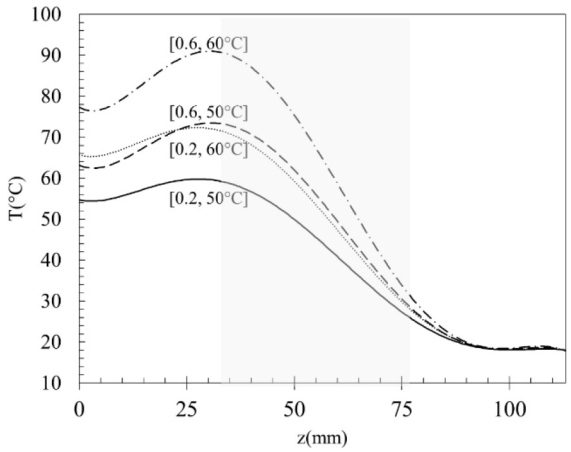



**Fig. 6-3.** Longitudinal temperature profiles of the film region at operating conditions [mass flow-rate, $T_{out}$] of experiments (1–4): Exp(1)-[0.2, 50]; Exp (2)-[0.6, 50]; Exp(3)-[0.2, 60]; Exp(4)-[0.6, 60].

operation, such an iteration loop is not necessary.

The resolution of the equation set is schematically given in Fig. 6-5. Inert molar flow rates ($L_s$, $G_s$), as well as composition variables at (z = 0) are first computed, as well as temperature dependent diffusivities and equilibrium data in order to derive the partial mass transfer coefficients and the chemical enhancement factor. The "flux-continuity" equation is solved to obtain the $CO_2$ molar fraction at the interface between the film and the membrane ($x^*_{f,l,j=0}$). The differential mass balance is then resolved after an explicit discretization scheme in order to compute the fraction of $CO_2$ dissolved in the solvent at the exit of the first elementary volume ($x_{j=1}$). The $CO_2$ fraction present in the gas entering in counter-current flow into the neighboring elementary volume is deduced from the operating curve. The free unreacted $CO_2$ in the liquid bulk phase and liquid film were calculated from the VLE equilibrium data. The model iterates along the fiber length until reaching the point corresponding to the solvent entrance at (z = L).

## 6.3. Results

### 6.3.1. Validating the two-profile approach

Coupling microwave heating to mass-transfer and chemical reaction is achieved by integrating two longitudinal temperature profiles in the 1D reactive mass-transfer model. How to define these temperature profiles starting from 3D T-maps was addressed, however we deemed it interesting to analyze the behavior of the simulated desorption flux using single T-profiles: either that of the bulk or of the stagnant film, and

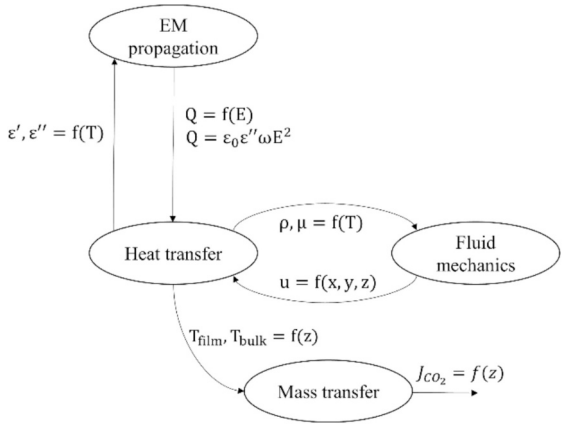



**Fig. 6-4.** Schematic of mass-transfer coupling to MW heating to simualte MW-assisted chemical desorption.

**Table 6-1**
Choice of T-profile in calculating physical and equilibrium properties in the non-isothermal chemical desorption model.

| Quantity | Temperature choice | Justification |
|---|---|---|
| VLE | Bulk | VLE relation is used for calculation of molecular $CO_2$ in the liquid bulk. |
| He | Bulk/film | Bulk temperature is used to determine the free unreacted $CO_2$ in the liquid bulk. Film temperature is used to determine free unreacted $CO_2$ in equilibrium with gas phase. |
| $D_{ETA\ in\ 30\ wt\%\ ETA+CO2}$ | Film | $D_{ETA}$ determines the transfer rate of ETA out of the reacting film. Hence it is dependent on the film temperature. |
| $D_{CO2\ in\ 30\ wt\%\ ETA+CO2}$ | Film | $D_{CO2}$ determines the transfer rate of $CO_2$ across the liquid film to reach the liquid-gas interface. Hence it is dependent on the film temperature. For cases of membrane wetting by solvent, $D_{CO2}$ is calculated from the film temperature. |
| $D_{CO2\ in\ N2}$ | Film | The porous membrane has been shown to have similar temperature as the hot liquid film. |
| $D_{CO2\text{-}knudsen}$ | Film | The porous membrane has been shown to have similar temperature as the hot liquid film. |

compare them to use of dual profiles. As a reminder, the operating conditions of experiments (1–8) of the experimental design are mentioned in Table 6-2.

We start by examining the desorption rates averaged over the cross-section of the fiber assuming radially uniform temperature that varies axially according to the film profile. Results in Fig. 6-6 show that the model overestimates the experimental average $CO_2$ desorption rate by a factor of five in comparison to experimental data. It can be suspected that the large discrepancy could also be caused by partial membrane wetting. To test this hypothesis, desorption was simulated considering different fractions of wetting in the membrane as shown in Fig. 6-7. The figure shows that despite the huge decrements of the computed desorption flux, the allure of the curves remains independent from the wetting fraction used. This shows that the occurrence of membrane wetting cannot account for the deviations observed in Fig. 6-6. In conclusion the exclusive use of the film T-profile in the numerical model is not appropriate to simulate MW-assisted desorption.

Fig. 6-8 compares the experimental desorption flux to that predicted by the model utilizing the "bulk" temperature profile. The figure shows that the predicted flux is of the same order of magnitude as the experimental, albeit it cannot correctly account for variations observed in the different operating conditions. The model is unable to account for the jump in the desorption flux at experiments between (2) and (4) or

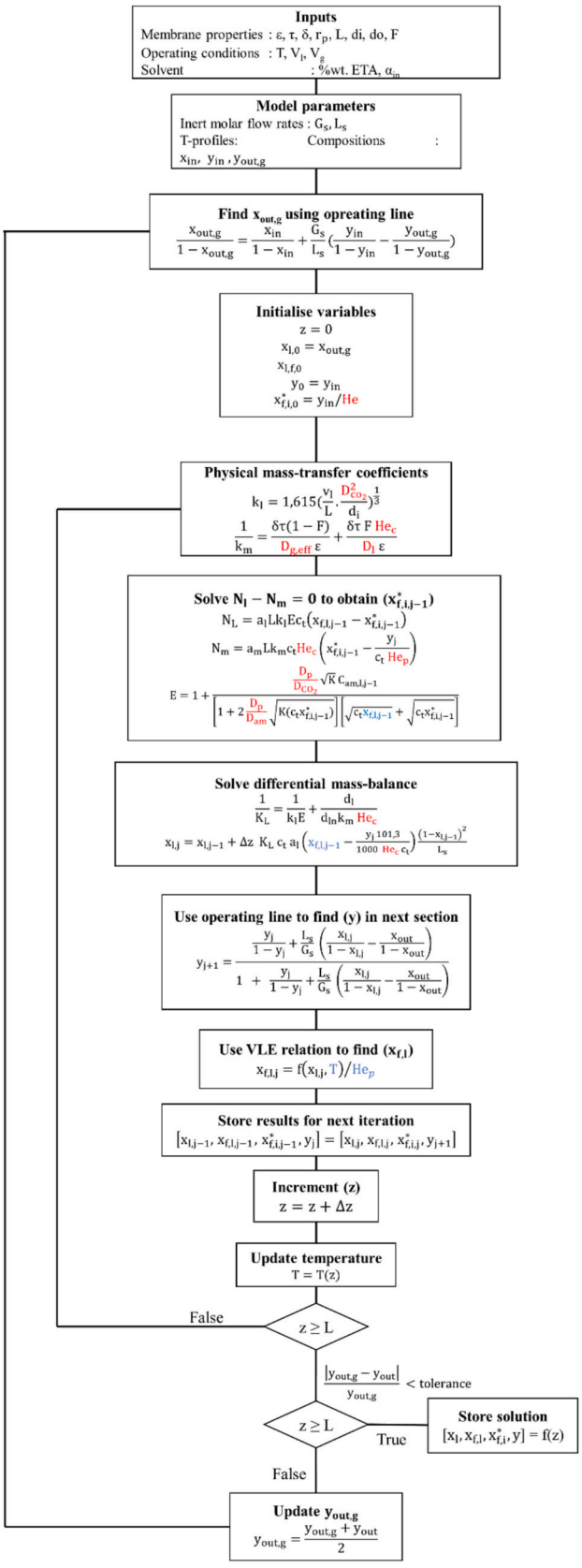



**Fig. 6-5.** Solving procedure of the microwave-assisted $CO_2$ desorption model.

**Table 6-2**
Operating conditions at experiments (1–8) of plan of experimental design.

| Experiment | $u_{g(mL/s)}$ | $v_{l(mL/s)}$ | $T_{out(°C)}$ |
|---|---|---|---|
| 1 | 3.33 | 0.2 | 50 |
| 2 | 3.33 | 0.2 | 60 |
| 3 | 3.33 | 0.6 | 50 |
| 4 | 3.33 | 0.6 | 60 |
| 5 | 6.66 | 0.2 | 50 |
| 6 | 6.66 | 0.2 | 60 |
| 7 | 6.66 | 0.6 | 50 |
| 8 | 6.66 | 0.6 | 60 |

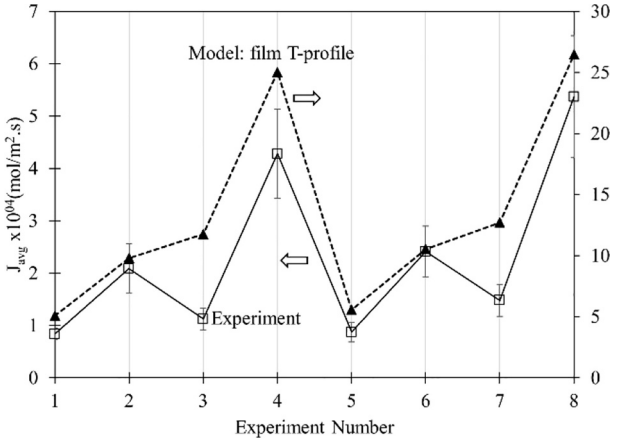



**Fig. 6-6.** Comparison of experimental desorption flux with the numerical model utilizing the "film" temperature profile and F = 0 %.

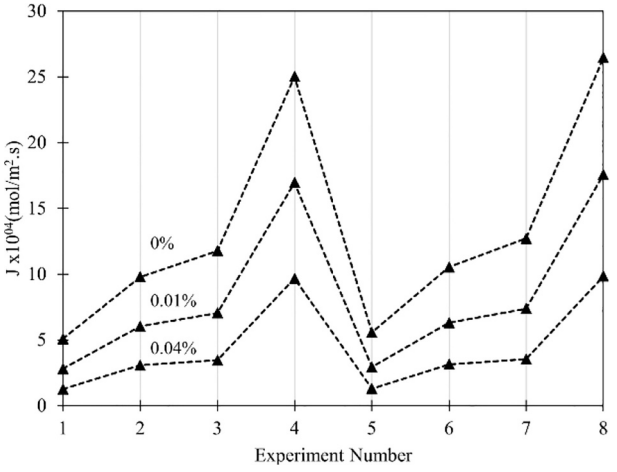



**Fig. 6-7.** Desorption flux with model utilizing "film" T-profile at different wetting fractions.

between (6) and (8). This is expected as the inversed T-gradients are not accounted for. Fig. 6-9 presents the average desorption flux when considering the two T-profiles (Bulk & film), in the manner previously highlighted. Despite the overestimation of the simulated data, the effects of the operating parameters on relative variations of the desorption flux appear better represented, especially at points (4) and (8). As a conclusion, the use of both temperature profiles is deemed appropriate, still, deviations between data sets persist nonetheless.

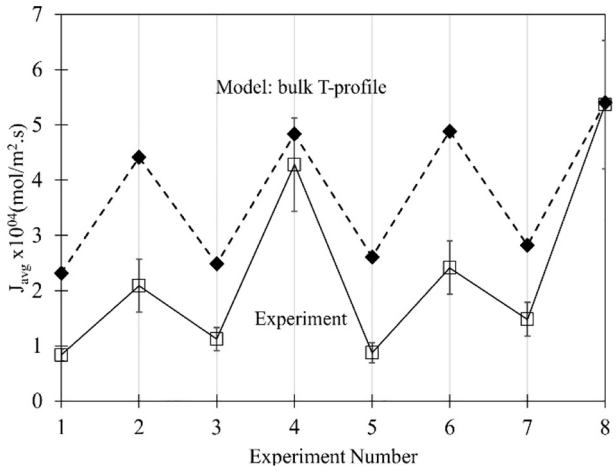



**Fig. 6-8.** Comparison of experimental desorption flux with the numerical model utilizing Bulk T-profile.

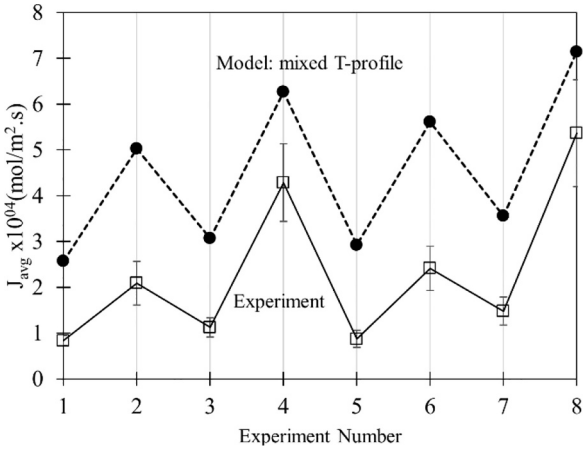



**Fig. 6-9.** Comparison of experimental desorption flux with the numerical model utilizing both bulk and film T-profiles.

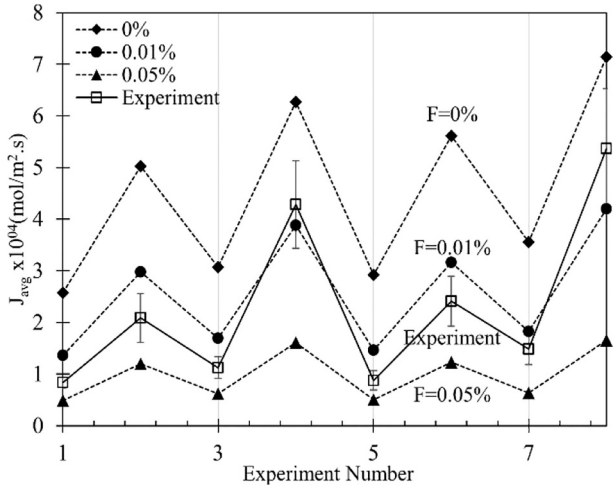



**Fig. 6-10.** Fitting numerical desorption flux to experimental values by adjusting the wetted fraction (F) of the membrane.

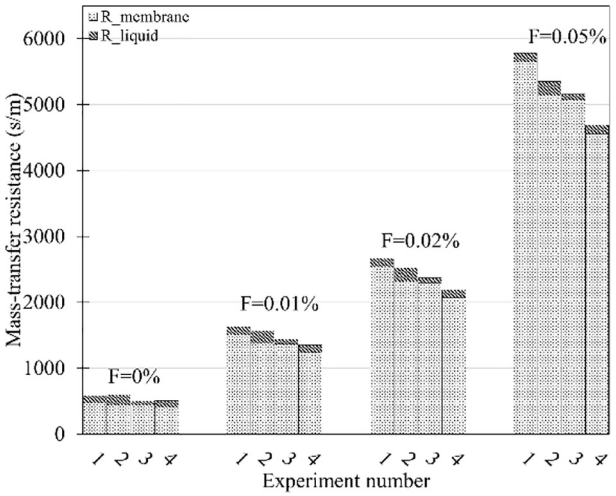



**Fig. 6-11.** Evolution of the resistance in the membrane and the liquid phase at different wetting fractions (F).

### 6.3.2. *Effect of partial membrane wetting*

It is suspected that deviation from experimental data in Fig. 6-9 is caused by the partial wetting of the porous structure that downgrades its performance with respect to experimental data. In this part, the sensitivity of the model towards the partial membrane wetting is examined.

The influence of wetted fraction on desorption is presented in Fig. 6-10. It is revealed that with even very low wetting fractions, the global desorption rates experiment significant decrements. One can also observe that the sensitivity to operating conditions decreases with increased wetting. The mass-transfer resistances are plotted in Fig. 6-11 where the membrane resistance dominates at all experimental conditions. It should be pointed out the even at no wetting the membrane has a thickness of 1 mm, this is higher than what is usually employed in membrane modules [58]. Consequently, the wetted fraction to produce the best fit with experimental desorption data is (F = 0.01): The predicted desorption seems to provide reasonably accurate estimation of the experimental desorption, but it is difficult to assert if the fitting indicates the occurring of wetting or if it is a lump term that counters other sources of error in the model. In this study the wetted fraction is taken to be independent from the operating conditions which may be untrue. Conversely, going with an assumption of a variable value of (F) would give an excellent agreement at each point; this however is to the detriment of extrapolating the numerical data to cases that aren't tested experimentally. It is interesting to note that the current model reproduced the experimental desorption rates however under the assumption that desorption is purely a thermal phenomenon.

The in-detail modeling of the temperature gradients revealed the elevated temperatures at the gas-liquid interface, which provides to some extent an explanation for the boosted desorption rates. This result points in the direction of discrediting the long discussed "non-thermal" effect that microwaves might have on reaction kinetics.

### 6.3.3. *Local desorption flux*

Fig. 6-12 shows the axial variations of the desorption rates computed along the whole fiber length. Desorption appears to be negligible in the first half of the microwave cavity region, at mid-cavity desorption rates steeply increase then reaches a plateau at the solvent exit. It appears that the useful surface area for desorption corresponds to half of the whole fiber under the tested conditions where the other half is not hot enough to overcome the equilibrium conditions with the gas phase. The cumulated desorption rates were plotted as function of the total surface area fraction in Fig. 6-13. The figure shows that cumulated desorption rates are identical for all experiments, and that 40 % of the fiber mass-transfer area is actually responsible for the total desorbed quantity. This result raises the question as to over which surface area should the average desorption flux be estimated, a question that is exclusive to microwave regeneration. Consideration of entire exchange area would negatively impact the estimation of the average desorption flux, thus clouding any advantages that this novel regeneration method might promise. This question was not explored any deeper, hence we base our estimations of average desorption flux on the entire surface of exchange including the sections outside the microwave applicator.

Further consideration of the desorption profiles in Fig. 6-12 shows the existence of negative flux for (z > 60 mm). This shows that on the cold side of the fiber, chemical absorption takes place, due the counter-current operation. The sweeping gas - being poor in $CO_2$ - contacts the hot solvent and thus desorption takes place; as it progresses along the fiber length it gets more and more enriched, simultaneously, up to a point where the partial pressure of $CO_2$ surpasses that in equilibrium with the solvent and chemical absorption occurs.

It is important to point out that, in general, isothermal membrane regeneration studies employ different operating conditions which makes it challenging to draw out clear conclusions as to which membrane, solvent, or process configuration are more efficient. When employing MW regeneration, comparison is rendered more difficult due to the delivery of MW power – an aspect of the process that is difficult to normalize.

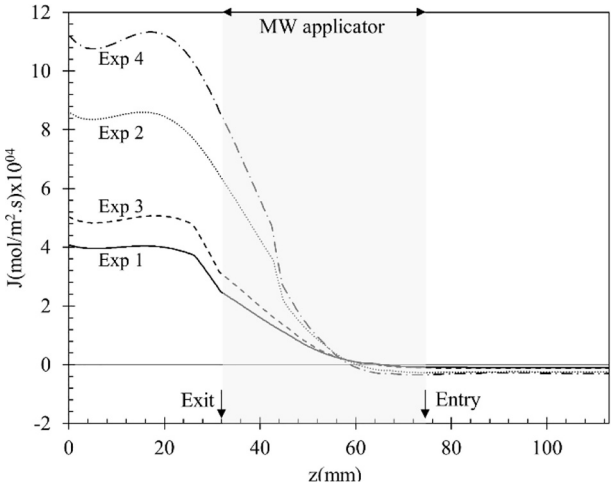



**Fig. 6-12.** $CO_2$ desorption profile as a function of the fiber position (Exp 1–4).

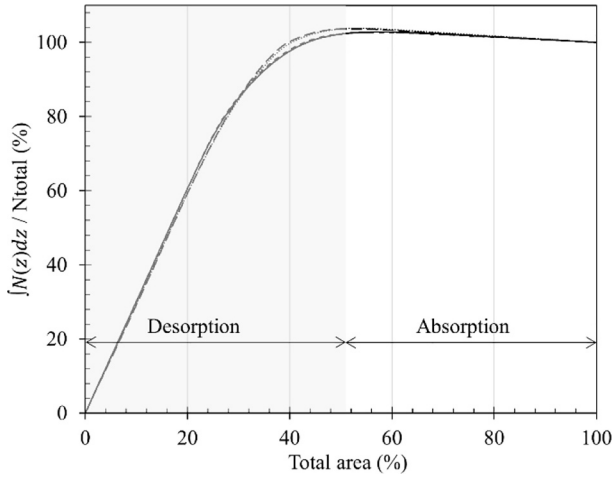



**Fig. 6-13.** Accumulated desorption rate function of the area for mass-transfer (Exp 1–4).

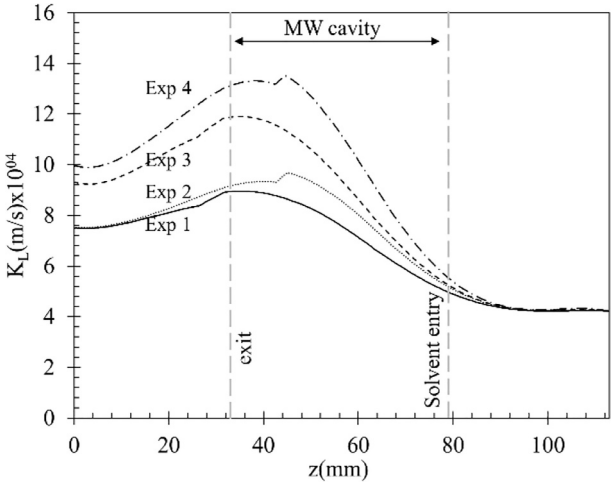



**Fig. 6-14.** Profile of overall transfer coefficient ($K_L$) function of the fiber length, (F = 0.01 %).

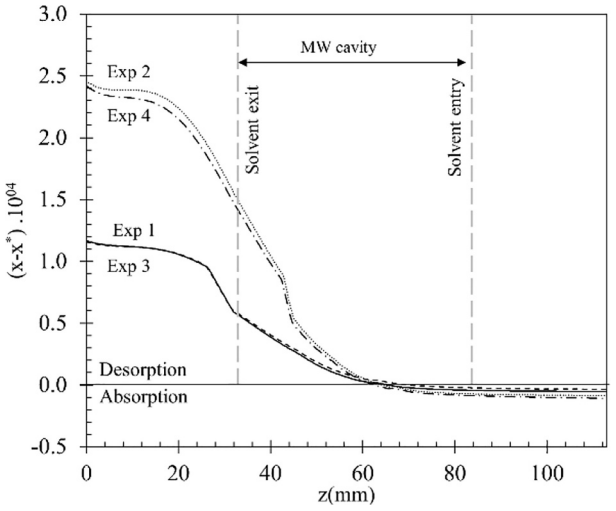



**Fig. 6-15.** Driving force for mass transfer ($x_{f,l} - x^*_{f,g}$) function of fiber length. Wetting fraction F = 0.01 %.

### 6.3.4. *Overall mass-transfer coefficient & mass-transfer driving force*

Desorption profiles observed in Fig. 6-12 depend on the driving force of mass-transfer and on the overall mass-transfer coefficient. We plot in Fig. 6-14 the profile of the overall transfer coefficient as function of the fiber length. For brevity of presentation, only results of experiments (1–4) are shown. The overall mass transfer coefficient does not experience great variations throughout the fiber length and is higher at the "hot" side of the fiber. It is interesting to note that variations of the overall mass transfer coefficient show a high degree of similarity to the film T-profile, but differs in the position of its maxima. The driving force was plotted in Fig. 6-15 for experiments (1–4), the driving force becomes significant at (z < 60 mm) which explains why desorption becomes active in this region. At the region of solvent entry, the driving force is negative indicating a $CO_2$ flux from the gas to liquid phases, hence chemical absorption. The discontinuities observed in the curves are caused by the interpolations on experimental VLE data.

Under the assumption of a uniform EM-dissipation in the solvent domain bounded by the MW cavity and as long as ($T_{out}$) is maintained constant, ($T_{bulk}$) is expected to be invariant at different fiber geometries or different solvent hydrodynamics as can be shown in Fig. 6-2 (experiments 1,3 or 2,4). Therefore, with regards to the driving force for mass-transfer no enhancement of this quantity is expected. This highlights

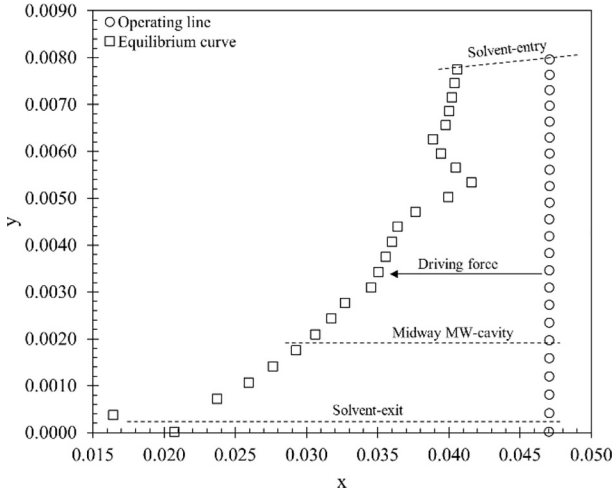



**Fig. 6-16.** Driving force diagram, case of isothermal regeneration at operating conditions of experiment (4), (F = 0.01 %).

that any potential of improvement proposed by MW-regeneration would mainly target the transfer coefficient ($K_L$), a conclusion that is subject to the assumption of chemical desorption being influenced only by temperature instead of a non-thermal effect.

We deemed it interesting to perform a comparison of the driving force between isothermal and non-isothermal regeneration (using MW irradiation). We plot both the operating line and the equilibrium curve in Fig. 6-16 and 1–66, corresponding respectively to the isothermal conditions. In isothermal regeneration the fiber volume was maintained at constant temperature which is the outlet temperature of the solvent from the microwave cavity ($T_{out}$ = 60 °C). Fig. 6-16 shows that driving force exists along the entire fiber length contrary for the non-isothermal mode where driving force becomes substantial after midway through the applicator. Towards the solvent exit region, the driving force increases in both modes to reach similar values at solvent exit. We point out that the use of experimental VLE data can cause some discontinuities in the equilibrium curve as observed in Fig. 6-16. In isothermal desorption the equilibrium curve and the operating line cannot intersect, however MW-regeneration demonstrates the opposite (Fig. 6-17). Towards the region of solvent entry, solvent temperature drops decrease the theoretical partial pressure of $CO_2$ in equilibrium with the liquid phase, resulting in chemical absorption on the cold side of the hollow fiber.

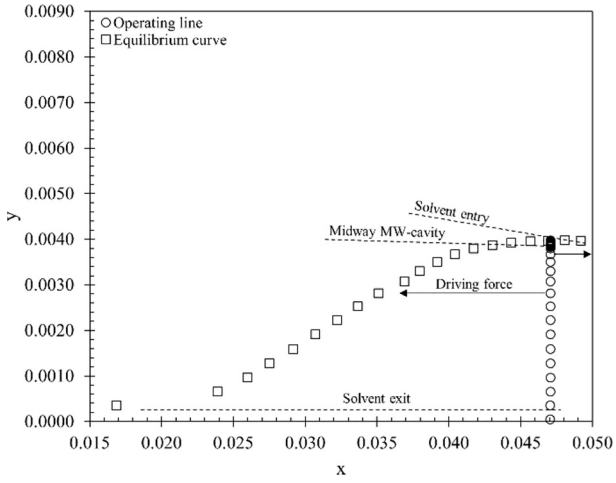



**Fig. 6-17.** Driving force diagram, case of microwave regeneration at operating conditions of experiment (4), (F = 0.01 %).

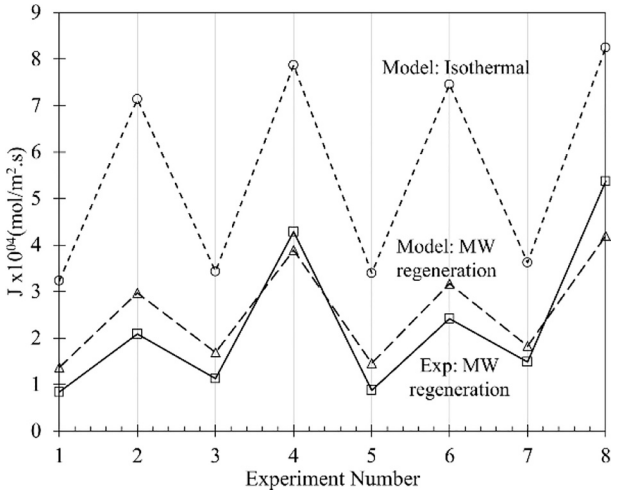



**Fig. 7-1.** Desorption flux under isothermal - ($T = T_{out}$) and non-isothermal regeneration - T = f(z). Wetting fraction (F = 0.01 %).

## 7. Complementary studies

### 7.1. MW-assisted versus isothermal regeneration

To evaluate the efficiency of MW regeneration, we compare it to the case of isothermal regeneration where a uniform temperature equal to that of the solvent outlet is applied. Fig. 7-1 presents the average $CO_2$ flux simulated in isothermal and MW conditions for a wetted membrane (F = 0.01 %), as well as the experimental results of MW-regeneration. The figure shows that the average desorption flux under isothermal regeneration conditions exceed those obtained with microwave radiation. However, it should be noted that the average desorption fluxes were computed over the entire length of the fiber. The entire length of the fiber was so assumed to be at the same temperature under isothermal conditions, whereas only a portion of this length was actually exposed to microwave irradiation within the cavity.

Plotting the local desorption rate profiles along the fiber highlights the significant variations induced by the unexposed surface fraction of the fiber upstream of the MW cavity. For instance, this profile is reported in Fig. 7-2 in case of experiment 4, and compared with the one simulated assuming isothermal conditions. Whilst local desorption rates are found nearly constant along the fiber in isothermal conditions, significant increases are denoted after the cavity entrance, in the region where the fiber is submitted to MW. A maximum of the local flux is denoted in the region corresponding to the cavity exit, which exceeds the isothermal data. In the region of (z < 35 mm), hotspots form in the liquid film with temperature rising up to 90 °C against 60 °C in the bulk flow (Fig. 4.8). These results indicate that such local temperature rises at the solvent-fiber wall interface hence result in an intensification of the mass transfer rates thanks to the direct molecular heating process induced by MW. A rigorous comparison between the two regeneration modes (isothermal-MW) would therefore require taking into account the pre-heating region of the fiber in both cases.

### 7.2. Effect of solvent preheating on desorption

It has been shown that the average desorption rates correlated positively with the solvent outlet temperature ($T_{out}$) and flow rate. In order to explore potential parameters that may improve desorption rates under MW mode, the impact of ($T_{in}$) on the performance of was assessed.

The inlet temperature ($T_{in}$) of the solvent was varied between [10–50 °C] by steps of 10 °C, other operating conditions were held constant at those of experiment (4). Film T-profiles are plotted in Fig. 7-3 function at varying $T_{in}$. Results show that as $T_{in}$ decreases, the "cold" side of the fiber becomes colder leading to lower film temperatures; the "hot" side of the fiber becomes hotter leading to increased film temperatures. It appears as well that all temperature curves have similar tendencies, locations of maxima and intersect at mid-cavity, independently from ($T_{in}$). The desorption profiles corresponding to different ($T_{in}$) were plotted in Fig. 7-4. The figure shows that greater of flux variations are observed when ($T_{in}$) is lower, i.e. for $T_{in}$ = 10 °C, desorption is highly impacted on the "cold" side, on the hot side, the local desorption flux is superior to all other cases. It can also be seen as $T_{in}$ increases, desorption flattens until reaching the isothermal case representing an almost constant desorption profile. Practically speaking, The local variations of (J) at ($T_{in}$ = 10 °C) do not amount to any improvement or deterioration of the average desorption flux as can be seen from Fig. 7-5. The observed changes in desorption profile along the fiber balance out such that on average, no change in global desorption performance is observed.

### 7.3. Effect of fiber radius on desorption flux

The hollow fiber used for desorption tests is of millimetric radius (2.15 mm), which is relatively large in comparison to those used in

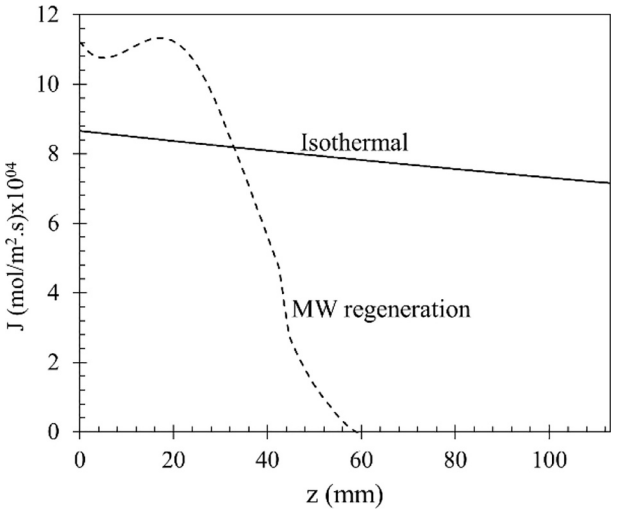



**Fig. 7-2.** Desorption flux: isothermal - ($T = T_{out}$) vs non-MW-regeneration. Operating conditions of experiment 4. Wetting fraction (F = 0.01 %).

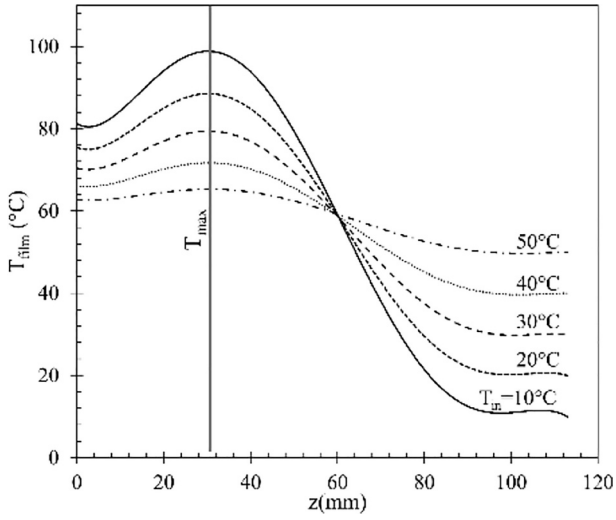



**Fig. 7-3.** Film T-profiles along the fiber for 30 wt% ETA solvent flow rate (0.6 mL/s) at different entry temperature $T_{in}$= [10,50], and $T_{out}$ = 60 °C.

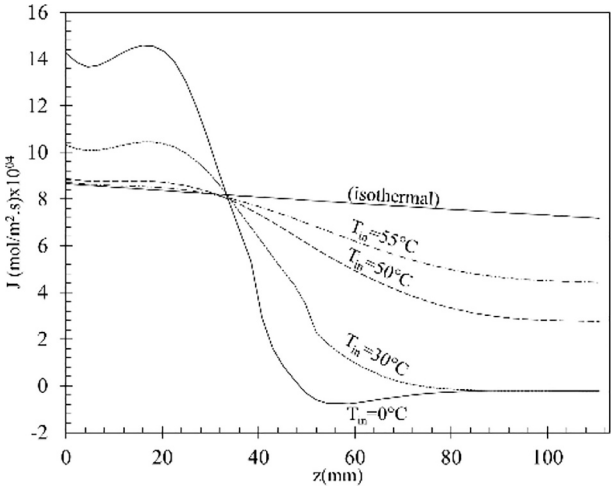



**Fig. 7-4.** Variations of local desorption rates along the fiber length for different entry temperature. F = 0.01 %, $T_{out}$ = 60 °C, solvent vl = 0.6 mL/s.

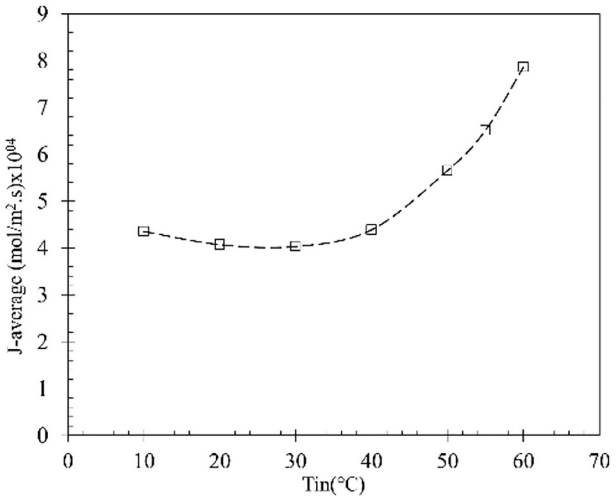



**Fig. 7-5.** Average desorption flux function of solvent entry temperature ($T_{in}$). F = 0.01 %, $T_{out}$ = 60 °C, solvent vl = 0.6 mL/s.

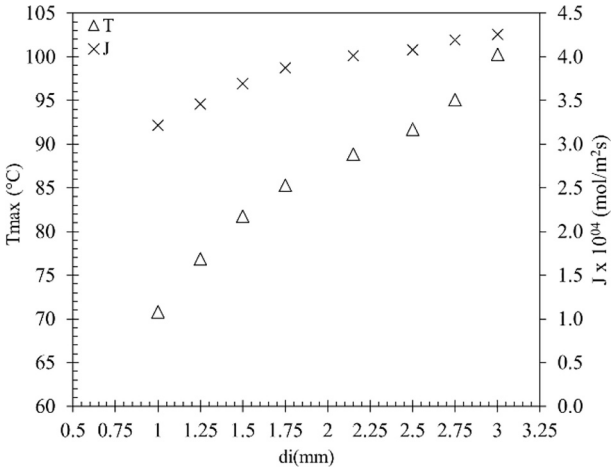



**Fig. 7-6.** $T_{max}$ and $J_{avg}$ for varying internal radii of the fiber. $T_{in}$ = 20 °C, $T_{out}$ = 60 °C, mass-flux = 4.9 g/cm$^2$.s, F = 0.01 %.

membrane modules. In order to take advantage of high interfacial surface density that membrane contactors might offer, the diameter of the fiber needs to be small. For this reason, the effect of the fiber size on the temperature distribution and the process performance needs to be explored.

For all tested cases, inlet and outlet temperatures were held constant at ($T_{in}$ = 20 °C) and ($T_{out}$ = 60 °C) respectively, in addition the solvent flow per unit area of cross-section was held constant. The T-maps were computed at different fiber radii: 1, 1.25, 1.5, 1.75, 2.15, 2.5, 2.75, and 3 mm. To simplify evaluation ($T_{max}$) was used as indicator of radial temperature gradients and was plotted as a function of the fiber radius in Fig. 7-6. The figure shows that $T_{max}$ follows increase with fiber dimensions. Consequently, this translates to an increase of ($J_{avg}$) with fiber radius as shown on the same figure.

In order to assess performance on the scale of a gas-liquid contactor, the height of transfer unit is a good indicator of the volumetric performance of the equipment. Starting from the differential mass-balance (5–21) we can deduce the expressions of the number of transfer units (NTU) and the height of the transfer unit (HTU) expressed in (7–1) and (7–2) respectively. In (7–2) ($v_l$) is the average solvent velocity over the entire section of the module, ($K_L$) is the average transfer coefficient, ($a_v$) the volumetric interfacial area as expressed in (7–3) with ($d_i$) and ($d_o$) being the inner and outer diameters of the fiber, and ($\phi$) is the volumetric fraction of the hollow fibers in the membrane module. Keep in mind that for our case, the fiber and the surrounding quartz tube constituted the membrane contactor.

$$NTU = \int_{x_{out}}^{x_{in}} \frac{dx}{(1-x_l)^2\left(x_{f,l} - x^*_{f,g}\right)} \tag{7-1}$$

$$HTU = v_l / K_L a_v \tag{7-2}$$

$$a_v = (4\phi d_i)/d_o^2 \tag{7-3}$$

The HTU is plotted as a function of the fiber radius in Fig. 7-7: The figure shows that increasing the radius of the fiber increases the height of the transfer unit, thus decreasing the volumetric desorption efficiency of the module. This shows that the improvement of the desorption flux from bigger fibers is outweighed by the loss in the volumetric density area; In simpler terms, the decrease in ($a_v$) beats the increase in ($K_L$). We hence conclude that using fibers of large size would not lead to an intensification of MW-assisted desorption.

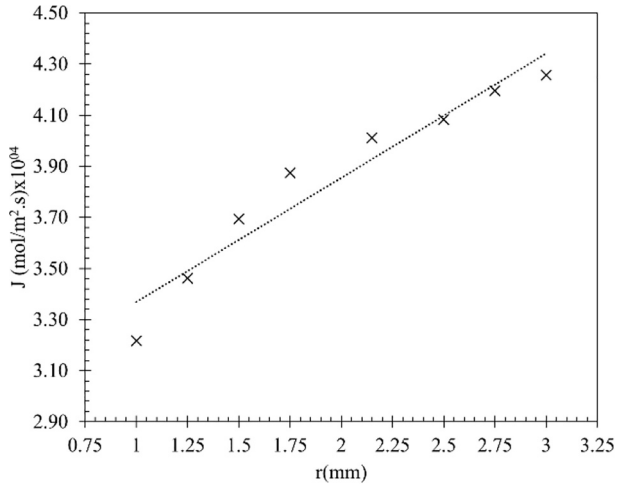



**Fig. 7-7.** Height of transfer unit function of the internal radius of the fiber. For all cases, $T_{in}$ = 20 °C, $T_{out}$ = 60 °C, mass-flux = 4.9 g/cm$^2$.s, and F = 0.01 %, $\phi$ = 0.85.

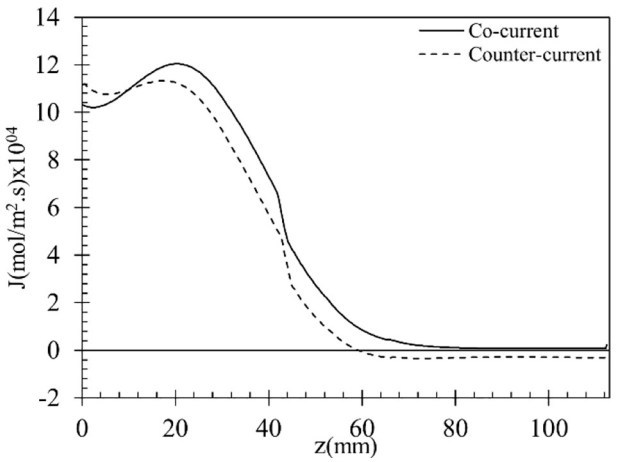



**Fig. 7-8.** Evolution of desorption flux along fiber length, co-current vs counter-current mode at operating conditions of experiment 4. $T_{out}$ = 60 °C, solvent vl = 0.6 mL/s, $\alpha_{in}$ = 0.44, gas flow = 3.33 mL/s.

### 7.4. Co-current versus counter-current operation

In Fig. 7-8 we plot the desorption flux along the fiber length, for both co-current and counter-current modes of operation. The co-current mode shows a very similar profile to the counter-current one. It is suspected that because the $CO_2$ concentration at the gas outlet is very low, changing the flow configuration of the gas phase would have no effect on performance, we also note that T-profiles are slightly affected by gaseous flow. *Co*-current flow differs from the counter-current, in that only desorption takes place instead of a mixed absorption- desorption process as seen in Fig. 7-8: in co-current operation, the sweeping gas contacts an ever-hotter solvent. It is true that in counter-current operation, absorbed $CO_2$ on the "cold" side of the fiber is almost negligible, nonetheless, this is exclusive to our work which involves a single fiber. When operating a membrane contactor in counter-current mode, the sweeping gas phase would be enriched in $CO_2$ when passing the "hot" side of the contactor; consequent $CO_2$ absorption is on the "cold" side of the contactor would be great enough to penalize the process performance. The average desorption flux for co-current and counter current modes are shown in Fig. 7-9. Overall the co-current mode achieved a better performance as no absorption seems to take place along the fiber length.

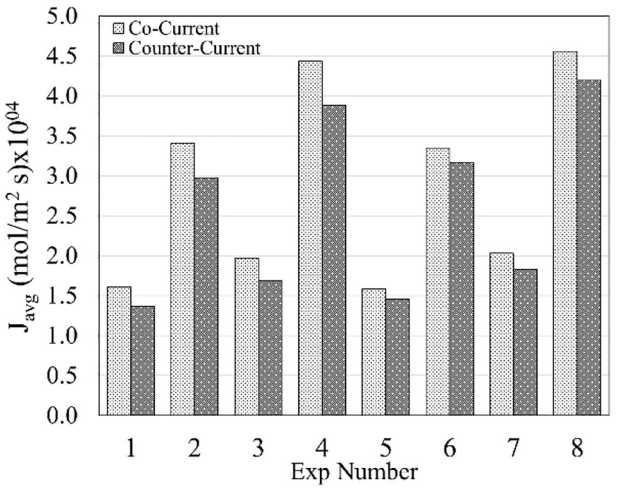



**Fig. 7-9.** Comparison of desorption performance between two modes of operation: co-current vs counter-current operation for solvent and sweeping gas flows.

### 7.5. Transposability to the scale of a membrane module

So far, the proposed numerical model was able to provide important insights into the operation of desorption under microwaves at the scale of an elementary fiber volume. It remains important nonetheless to examine its ability to predict process operation at the membrane module scale. To extrapolate the 1D simulation to a membrane system, it would be necessary to assume that all fibers within the bundle behave similarly. However, such an approach is unlikely to be valid as the electric field is expected to vary spatially across the radial section of the fiber bundle, giving way to temperature heterogeneities of the solvent flow over the module cross sectional area. It would also be numerically very demanding to account for local electric field variations and to simulate the thermal behavior of hundreds or thousands of millimetric fibers. To achieve radial temperature uniformity throughout the fibers, it is possible to design an optimal microwave applicator, whose module diameter must be sufficiently small in relation to the penetration depth of the microwaves. Another approach to overcoming the numerical cost issue would be to represent the fiber bundle as a pseudo-homogeneous medium, with effective dielectric and porous properties. The effective dielectric data should then be experimentally derived, or estimated from dielectric mixing laws. In addition, the desorption process model should be completed with the modeling of the phenomena that could be reasonably neglected at the local scale i.e. partial solvent evaporation and endothermic effect due of the $CO_2$ desorption process.

## 8. Sensitivity analysis of $CO_2$ desorption rates

### 8.1. Objectives and motivation

It has been established that the proposed model is able to predict fairly well the MW regeneration in a hollow fiber membrane. However, it remains necessary to evaluate the model sensitivity with respect to its parameters so that future efforts can be efficiently channeled in improving process performance. Another advantage of this analysis is to quantify the accepted accuracy in estimating physical, chemical, and transfer properties. The sensitivity study was conducted with respect to the membrane properties, the transfer and equilibrium properties of $CO_2$-ETA system, and the operating conditions as presented in Table 8-1. We note that each parameter was changed over a tight range to so that T-maps are assumed unaffected; otherwise analysis would drastically be more complex.

Membrane properties include those pertaining to the morphology of the porous media, and fiber dimensions which influence mass-transfer as well as hydrodynamic conditions respectively. The transfer or chemical properties include the diffusivities of $CO_2$ in the solvent and membrane presented by ($D_{CO2\text{-}l}$) and ($D_{CO2_eff_g}$) respectively, the diffusivity of ETA in the solvent ($D_{ETA\text{-}l}$), physical solubility of $CO_2$ in the solvent (He) as well as the VLE. Operating conditions include average liquid ($v_l$) or gas ($v_g$) volumetric flow rates, carbonation ration at entry ($\alpha_{in}$), composition of the sweeping gas at entry ($y_{in}$), as well as bulk ($T_b$) and film ($T_f$) profiles. We note that the quantities (E) and ($k_l$), although completely dependent on other physical quantities or operating conditions, were included in this study as this puts in question errors that result from the inherent assumptions used in deriving them.

**Table 8-1**
quantities used to evaluate the sensitivity of the desorption flux.

| Membrane properties | Physical properties | Operating conditions |
|---|---|---|
| $\xi$ | $D_{CO2_l}$ | $v_l$ |
| $\tau$ | $D_{ETsA_l}$ | $v_g$ |
| $r_i$ | $D_{CO2_eff_g}$ | $\alpha_{in}$ |
| $d_o$ | VLE | $y_{in}$ |
| $d_i$ | He | $T_{film}$ |
| | E | $T_{bulk}$ |
| | $k_l$ | |

### 8.2. Methodology and equations

The sensitivity of the desorption flux was evaluated by applying a perturbation to each tested quantity. Each quantity was changed in the range [−10 %, +10 %] with respect to the base value, and with a step of 2 % to give a total of 11 points. This procedure was performed over experiments (1–4), which results in a total of (8 × 11) average desorption flux data.

The relative average desorption rate ($J_{avg_R}$) was calculated relative to the base case as per (8–1). ($J_{avg}$) is the average desorption flux over the fiber surface, (P) being the factor that adjusts the value of a given quantity. The subscript ($_R$) stands for relative, i.e. relative to the base case. As an example, ($P = 1$) is the case where the tested parameter is not varied from the reference case, ($P = 1.1$) represents an increase of 10 % relative to the base value of that parameter. For ease of presentation, variations in the flux (J) were normalized with respect to the base case (P = 1) and expressed in percentage points.

$$J_{avg_R}\big|_{Exp(i),P} = \frac{J_{avg}\big|_{Exp(i),P} - J_{avg}\big|_{Exp(i),P=1}}{J_{avg}\big|_{Exp(i),P=1}} \text{ x } 100 \quad (8\text{-}1)$$

For a given tested parameter and value (P), the mean relative average desorption flux $\overline{J}_{avg_R}$ was obtained from the eight experiments (1–8) as expressed in (8–2).

$$\overline{J}_{avg_R}\big|_P = 1/8 \sum_{i=9}^{i=16} J_{avg_R}\big|_{Exp(i),P} \quad (8\text{-}2)$$

The local sensitivity of the mean average relative flux at a given adjustment (P) of a given parameter, is denoted by ($\overline{\Delta J}_{avg_R}\big|_P$) as expressed in Eq. (8-3). This formulation gives 9 estimations of the local sensitivity: P belongs to the range [0.92–1.08] as the sensitivity cannot be determined at points ($P = 0.9$) and (P = 1).

$$\overline{\Delta J}_{avg_R}\big|_P = \frac{\overline{J}_{avg_R}\big|_{P+0.02} - \overline{J}_{avg_R}\big|_{P-0.02}}{0.04 \text{ x } 100} \quad (8\text{-}3)$$

The total average relative sensitivity ($\overline{\Delta J}_{avg_R_t}$) with respect to a parameter can be calculated as shown in (8–4) by averaging the obtained estimations of the local sensitivities at different perturbations.

$$\overline{\Delta J}_{avg_R_t} = 1/9 \sum_{P=0,92}^{1,08} \overline{\Delta J}_{avg_R}\big|_P \quad (8\text{-}4)$$

### 8.3. Membrane properties

The sensitivity to membrane properties is presented in Fig. 8-1, where the mean relative flux ($\overline{J}_{avg_R}$) was plotted with respect to the factor (P). Fig. 8-1 shows that membrane porosity is the most influential parameter, i.e. an increase of (10 %) raises the desorption flux by (17 %) relative to the average base value. The internal diameter ($d_i$) influences the liquid phase mass transfer coefficient, while ($r_p$) holds the lowest influence as it is responsible for decreasing the effective diffusivity of $CO_2$ in the porous media. The tortuosity is shown to have a negative influence on desorption as it increases the path traveled by $CO_2$ molecule to reach the sweeping gas.

### 8.4. Transfer and equilibrium properties

The mean relative flux ($\overline{J}_{avg_R}$) with respect to liquid mass transfer coefficient, physical solubility and vapor-liquid equilibrium properties is shown in Fig. 8-2. The vapor-liquid equilibrium is shown to have the greatest influence followed by the effective diffusivity of $CO_2$ in the gas phase ($D_{CO2\text{-}eff}$). This is not surprising as even under non-wetted condition; the membrane presents the biggest resistance to mass-transfer. Increase in $CO_2$ diffusivity in the liquid phase is found to negatively impact desorption performances, because as diffusivity increases, $CO_2$ concentration in the reactive film becomes similar to that in the bulk of the solvent thus chemical desorption reaction is less active. Increased diffusivity of ETA has a positive impact on desorption, this is due to the fact that the liquid film is richer in ETA than the liquid bulk, consequently greater diffusivity of ETA helps evacuate the produced ETA which helps shift the chemical reaction to the products side. It is also worth noting that, in the numerical model, the diffusivities of $ETAH^+$ and $ETACOO^-$ were assumed identical to that of ETA. Therefore, increased diffusivity allows faster diffusion of these reactants from the solvent bulk into the reactive film. Fig. 8-2 also shows that desorption has negligible sensitivity to henry's law, however it is very sensitive with respect to the equilibrium of 30 wt% ETA-$CO_2$ system.

### 8.5. Operating conditions

The mean relative change in desorption flux is plotted in Fig. 8-3 with respect to changes in the operating conditions. The carbonation ratio holds the greatest effect on desorption rates, it is followed by bulk temperature as it increases the concentration of free $CO_2$ in the bulk. The film temperature on the other hand - used for calculation of transfer properties, transfer coefficients and enhancement factor – follows the same trend as the bulk temperature but with a lower impact. (See Fig. 8–4.)

These results indicate that the carbonation ratio needs to be determined with a high degree of accuracy. They also show the importance of careful prediction of ($T_{bulk}$) profiles, and the necessity of precise

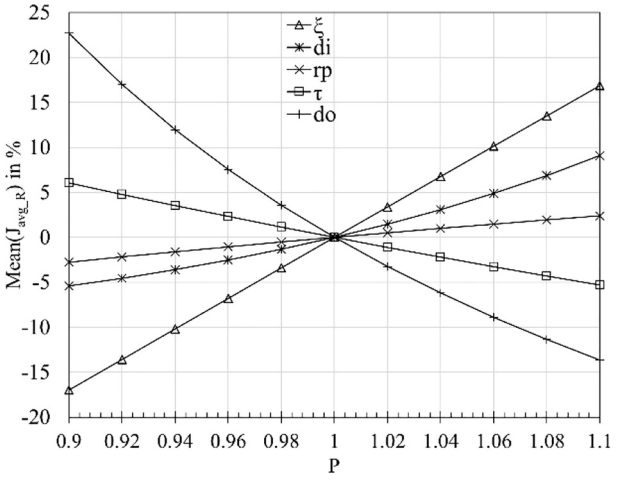



**Fig. 8-1.** Sensitivity curves of the desorption flux with respect to the change in membrane properties.

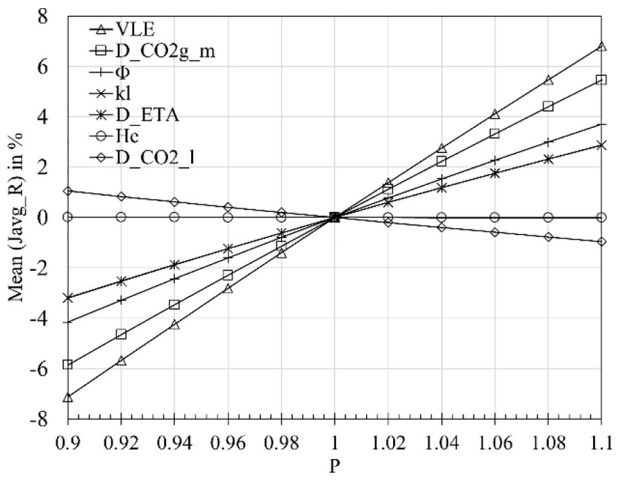



**Fig. 8-2.** Sensitivity curves of the desorption flux with respect to the change in physical or equilibrium properties.

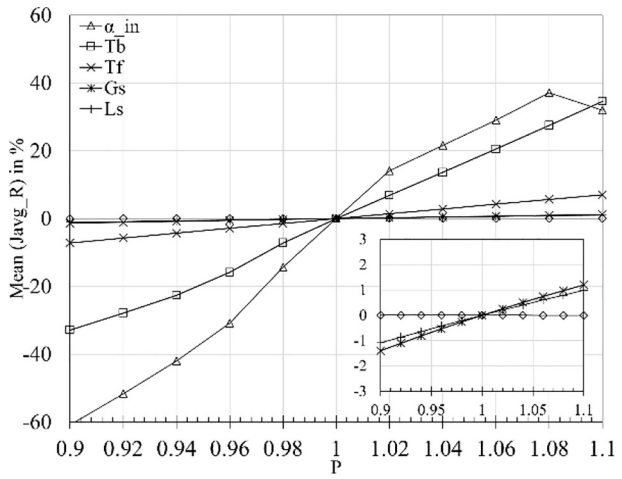



**Fig. 8-3.** Sensitivity curves of the global desorption flux with respect to operating conditions.

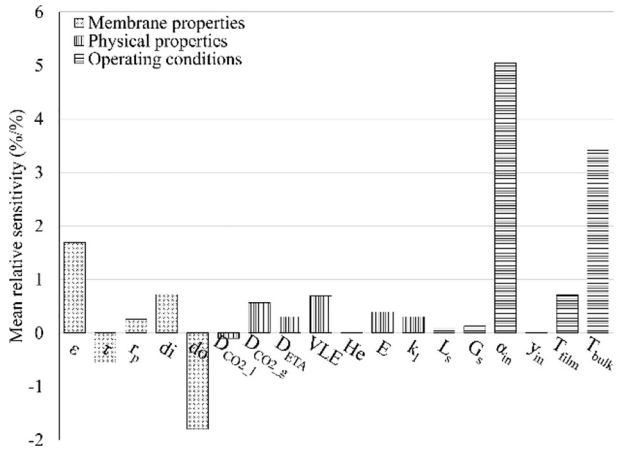



**Fig. 8–4.** Mean sensitivity of the desorption flux with respect to quantities pertaining to membrane properties, physical properties of the solvent, and operating conditions.

modeling of heat transfer in a microwave cavity. Liquid and gas flow rates have little contribution on desorption performance in comparison to other quantities, liquid velocity only contributes to the liquid mass transfer coefficient, but in a small manner as it is raised to the power of (1/3) in the Graetz-Lévêque correlation.

### *8.6. Recommendations*

The overall mean parameter sensitivities were calculated are plotted in Fig. 8–4. With regards to the membrane properties, it is recommended to choose a highly porous membrane material with small pore sizes as this would prevent liquid intrusion all while ensuring a good regeneration performance. With regards to the solvent properties, accuracy in determining (He) can be neglected as this has little impact on desorption, while ($D_{CO2\text{-}l}$) and ($D_{CO2\text{-}g}$) can be estimated with mild accuracy. In view of the moderate effect of VLE, data can be estimated with mild accuracy. Still, VLE data experience logarithmic variations with carbonation ratio or with temperature, therefore it holds the greatest effect on desorption rates amongst the other physical quantities. Sensitivity with respect to the operating conditions underlines the great improvement of desorption performance using high solvent carbonation ratios at entry. Fig. 8–4 reveals that desorption is highly sensitive to ($T_{bulk}$), the film temperature on the other hand depends on $T_{bulk}$ as well as several parameters mainly the solvent flow rate, and fiber diameter.

## 9. Conclusion

In this work, a multi-physical model was conceived to simulate MW desorption of $CO_2$ from 30 wt%ETA solvent circulating in the lumen of a porous PTFE hollow fiber membrane. The hollow fiber was placed concentrically in a quartz tube and the ensemble was placed in a monomode microwave cavity. A progressive complexification approach was adopted in which physical phenomena were independently simulated and experimentally validated. Numerical modeling of the electromagnetic fields in the microwave cavity shows the electric field to be homogeneous. To simulate the dissipation of microwaves in the solvent stream, heat and momentum transfers were integrated into the electromagnetic field propagation model so that 3D T-maps of the solvent flowing along the fiber could be determined. The latter highlight the occurrence of strong local temperature gradients in the liquid film region close to the membrane wall of the hollow fiber. Mass-transfer modeling in a hollow fiber membrane was based on the 1D resistance-in-series model which accounts for the acceleration effects due to chemical reactions, and for the decrement of the desorption rates caused by partial wetting of the membrane. The model simulates the local desorption rates along the axial direction of the hollow fiber according to temperature changes within the solvent bulk and film respectively. To simulate the microwave desorption process, the 3D temperature maps obtained in the MW cavity were transformed into two 1D temperature profiles that represent the variations of temperature along the fiber length in both the liquid film and bulk. The model was able to reproduce the experimental global desorption rate data with good accuracy, under the assumption that high local desorption rates induced by microwaves only result from thermal effects. This supposes to negate the said non-thermal effects that microwave fields might have on desorption kinetics.

Desorption fluxes along the axial direction of the fiber show that desorption onsets beyond a region close to the cavity entrance, where the solvent temperature is rising from ambient and is not large enough to activate the desorption process. A comparison with performance computed in isothermal conditions enlightens the intensification of the desorption process resulting from the hot spots induced by microwave selective heating within the liquid film at the interface between the membrane wall and the solvent flow. Complementary studies suggest that co-current mode of operation may be more advantageous than the counter-current one due to the occurrence of $CO_2$ absorption at cold regions of the fiber. Furthermore, increasing the fiber diameter was shown to improve the global desorption rates, however at the expense of volumetric efficiency. At last, according to the model parameter sensitivity study, it was found that the solvent bulk temperature, its carbonation ratio and chemical equilibrium data are the main drivers of the process performance predictions.

## CRediT authorship contribution statement

**A. Hajj:** Writing – review & editing, Writing – original draft, Methodology, Investigation, Formal analysis, Data curation, Conceptualization. **S. Curet:** Writing – review & editing, Writing – original draft, Visualization, Validation, Supervision, Software, Resources, Methodology, Investigation, Funding acquisition, Formal analysis, Data curation, Conceptualization. **P. Pré:** Writing – review & editing, Writing – original draft, Visualization, Validation, Supervision, Software, Resources, Project administration, Methodology, Investigation, Funding acquisition, Formal analysis, Data curation, Conceptualization.

## Declaration of competing interest

The authors declare that they have no known competing financial interests or personal relationships that could have appeared to influence the work reported in this paper.

**Acknowledgements**

The authors gratefully acknowledge the National Research Agency (ANR) of France for their grant (19-CE05-0027-01, WAVEINCORE project), as well as the French National Association for Research and Technology (ANRT, CIFRE agreement 2020/0193).

## Appendix A. Appendix

### A.1. Electromagnetic modeling: Dielectric properties

#### A.1.1. Dielectric properties of porous PTFE fiber

The relative permittivity of porous PTFE fiber is determined using the Landau-Lifshitz-Looyenga dielectric mixing law [59]; the law is used to calculate the apparent dielectric properties of a dispersed phase in a continuous phase. The equation is given in (A-1) with ($\varepsilon^*$) being the complex permittivity of the mixture, ($\varepsilon_1^*$) complex permittivity of the continuous phase, ($\varepsilon_2^*$) complex permittivity of the dispersed phase, and (v) being the volumetric fraction ($v_1 + v_2 = 1$).

$$(\varepsilon^*)^{1/3} = v_1(\varepsilon_1^*)^{1/3} + v_2(\varepsilon_2^*)^{1/3} \tag{A-1}$$

#### A.1.2. Dielectric properties of distilled water

The Debye model was used for calculation of the dielectric properties of distilled water. The dispersion parameters function of temperature were obtained from previous authors [60]. Validity of these parameters are for T ϵ [0, 55] °C and in the frequency range f < 20.05GHz. The complex permittivity is given by the Debye model:

$$\varepsilon' - j\varepsilon'' = \varepsilon_\infty + \frac{\varepsilon_0 - \varepsilon_\infty}{1 - i2\pi\tau f} + \frac{i\sigma}{2\pi\varepsilon_0^* f} \tag{A-2}$$

The relative static dielectric constant is given by the following expression:

$$\varepsilon_0 = 87,85306\exp(-0,00456992\,T) \tag{A-3}$$

The relaxation time is given by:

$$\tau(ps)^{-1} = 5.631\,10^{-02} + 2.12\,10^{-03}T + 1.86\,10^{-05}T^2 \tag{A-4}$$

The optical relative dielectric constant is given by:

$$\varepsilon_\infty = 6,49 - 0,025\,T(^\circ C) \tag{A-5}$$

#### A.1.3. Dielectric properties of 30 wt%ETA

The dielectric properties of 30 wt% ETA used in the MW heating model are displayed in Table A1 over the temperature range [20–80 °C], and the carbonation ratio [0.2–0.55] from [33]. Linear interpolation was used to estimate the properties within and outside the measurement ranges of temperature and carbonation ratio.

**Table A1**
Relative permittivity (ε') and loss factor (ε") of 30 wt% ETA at 2.45GHz.

| α | T(°C) | ε' | ε" |
|---|---|---|---|
| 0 | 20 | 61.5 | 18.8 |
| 0 | 60 | 56.9 | 9.1 |
| 0.22 | 20 | 56.04 | 34.19 |
| 0.22 | 30 | 57.29 | 34.33 |
| 0.22 | 40 | 57.95 | 35.45 |
| 0.22 | 50 | 58.27 | 37.49 |
| 0.22 | 60 | 57.78 | 39.79 |
| 0.22 | 70 | 56.92 | 42.71 |
| 0.22 | 80 | 55.94 | 46.78 |
| 0.33 | 20 | 56.54 | 39.68 |
| 0.33 | 30 | 58.27 | 41.52 |
| 0.33 | 40 | 59.33 | 44.42 |
| 0.33 | 50 | 59.69 | 47.73 |
| 0.33 | 60 | 59.33 | 52.27 |
| 0.33 | 70 | 58.88 | 56.62 |
| 0.33 | 80 | 56.44 | 59.48 |
| 0.44 | 20 | 57.04 | 45.66 |
| 0.44 | 30 | 58.64 | 48.43 |
| 0.44 | 40 | 60.22 | 53.51 |
| 0.44 | 50 | 60.93 | 58.26 |
| 0.44 | 60 | 61.18 | 63.50 |
| 0.44 | 70 | 61.01 | 68.96 |

(*continued on next page*)

**Table A1** (*continued*)

| α | T(°C) | ε' | ε'' |
|---|---|---|---|
| 0.44 | 80 | 61.54 | 74.43 |
| 0.55 | 20 | 56.42 | 50.92 |
| 0.55 | 30 | 58.53 | 55.29 |
| 0.55 | 50 | 59.12 | 64.84 |
| 0.55 | 60 | 59.08 | 69.10 |
| 0.55 | 70 | 61.59 | 74.29 |
| 0.55 | 80 | 61.23 | 78.43 |

### *A.2. Thermal and physical properties:*

#### *A.2.1. Thermal conductivity of 30 wt% ETA*

The thermal conductivity of 30 wt% ETA was fitted by Ghasem [61] using the Filippov equation of a binary mixture presented in (A-6). (λ) is the thermal conductivity of pure component in (W/m K), ($w_1$) and ($w_2$) are the weight fractions of ethanolamine and water respectively, (K) is a fitting constant taken as (K = 0.72) for aqueous ethanolamine solution. The correlation is valid for a molar fraction ($x_{ETA} < 0.1$) and at $T = 25$ °C. Despite its limited validity, it was used in the current multi-physical model due to lack of better data.

$$\lambda_m = w_1\lambda_1 + w_2\lambda_2 - Kw_1w_2(\lambda_2 - \lambda_1) \quad \text{(A-6)}$$

The thermal conductivity of pure ETA is determined from the correlation proposed by Shokouhi [62] and presented in (A-7) for a validity range of $30 < T < 80$ °C.

$$\lambda_{MEA} = -0,1711T + 291,2846 \quad \text{(A-7)}$$

The thermal conductivity of DW is determined from correlation (A-8), taken from [63].

$$\lambda' = -1,48 + 4,12T^2 - 1,63T^2 \quad \text{(A-8)}$$

#### *A.2.2. Specific heat of 30 wt% ETA solution*

The specific heat of aqueous ethanolamine was calculated from the correlation of Kim [64] for loaded and fresh solutions of aqueous ethanolamine. The expression of the specific heat is given in equation (A-9), and the pertaining constants are listed in Table A2 for different ETA mass fractions, and carbonation ratios. Equation (A-9) is valid for 30 °C < $T$ < 80 °C, for temperatures outside this range linear extrapolation was used. Linear interpolation was used to determine the specific heat at carbonation ratios bounded by α = 0 and α = $\alpha_{max}$.

$$C_p\left(J.g^{-1}K^{-1}\right) = a + bT \quad \text{(A-9)}$$

**Table A2**
Parameters for the calculation of specific heat of aqueous ethanolamine solutions.

| % wt. ETA | Carbonation ratio | a | b x $10^{03}$ |
|---|---|---|---|
| 20 | Fresh solution | 3.1315 | 2.8479 |
| | 0.634 | 2.247 | 4.4044 |
| 22.5 | Fresh solution | 3.0666 | 2.8945 |
| | 0.616 | 2.1374 | 4.5492 |
| 25 | Fresh solution | 2.9523 | 3.1530 |
| | 0.597 | 1.9983 | 4.8434 |
| 30 | Fresh solution | 2.5661 | 4.1847 |
| | 0.581 | 1.8252 | 5.0097 |

It is worth mentioning that as we rely on interpolating, this is not without justification. To our knowledge, the only other author who reported the specific heat of aqueous ETA solution at different carbonation ratios, was Weiland [65]; unfortunately, his data are limited to ambient temperatures which limits their utility.

#### *A.2.3. Density of 30 wt% ETA solution*

Weiland [66] measured the density of aqueous solutions of single and blended alkanolamine aqueous solutions at different temperatures and carbonation ratios. The author used experimental data along with data collected from ten different sources to establish the density correlation valid for several amines, over the temperature range [273–398 K°] and the carbonation ratio (α < 0.6).

The density is presented in (A-10) with subscript (AM) representing amine, (x) is the mole fraction, (M) is the molar mass, (V) is the molar volume of the solution.

$$\rho = [x_{AM}M_{AM} + x_{H2O}M_{H2O} + x_{CO2}M_{CO2}]/V \quad \text{(A-10)}$$

The molar volume of the solution (mL/mol) is expressed in (A-11) with (V*) being null for the case of ETA, while (V**) being the excess molar

volume from two component interactions is expressed in (A-12) for ETA. The constants "e", and "d" are found in Table A3.

$$V = x_{AM}V_{AM} + x_{H2O}V_{H2O} + x_{CO2}V_{CO2} + x_{AM}x_{H2O}V^{*} + x_{AM}x_{CO2}V^{**} \quad \text{(A-11)}$$

$$V^{**} = d + ex_{Am} \quad \text{(A-12)}$$

The molar volume of amine is presented in (A-13), with ($V_{AM}$) expressed in (mL/mol), (T) is in K°, with the constant "a", "b", "c" being expressed in Table A3.

$$V_{AM} = M_{AM}/\left[a\,T^2 + bT + c\right] \quad \text{(A-13)}$$

The molar volume of $H_2O$ (mL/mol) was calculated from (A-14) and has a validity range [273–648 K°]. The constants A, B, C, D are presented in Table A3.

$$\rho_{H2O} = a \Big/ b^{1+\left(1-\frac{T}{c}\right)^{d}} \quad \text{(A-14)}$$

**Table A3**
Constants for calculation of molar and excess volumes.

| | MEA | DEA | MDEA | $H_2O$ |
|---|---|---|---|---|
| a | -5.35E-07 | -6.91E-07 | -4.68E-07 | 0.14395 |
| b | -4.51E-04 | -2.07E-04 | -4.25E-04 | 0.0112 |
| c | 1.194 | 1.217 | 1.205 | 649.727 |
| d | 0 | 0 | 12.983 | 0.05107 |
| e | 0 | 0 | 397.72 | – |

### *A.2.4. Viscosity of 30 wt% ETA solution*

The viscosities of partially carbonated aqueous amine solutions were measured and correlated in [66] according to equation (A-15). The validity of this correlation extends to the temperature range [273–398 K°], a carbonation ratio ($\alpha < 0.6$), and for an amine mass fraction ($\Omega < 40$ %). The constants in equation (A-15) are presented in Table A4 for three different alkanolamines.

$$\frac{\mu_{soln}}{\mu_{H2O}} = \exp\left[\left[(a\Omega + b)T + (c\Omega + d)\right]\left[\alpha(e\Omega + fT + g) + 1\right]\Omega/T^2\right] \quad \text{(A-15)}$$

**Table A4**
Fitting constants for the viscosity of amine solvents.

| | ETA | DEA | MDEA |
|---|---|---|---|
| a | 0 | −0.0724 | −0.1944 |
| b | 0 | −3.4363 | 0.4315 |
| c | 21.186 | 54.319 | 80.684 |
| d | 2373 | 3628 | 2889.1 |
| e | 0.01015 | −0.0015 | 0.0106 |
| f | 0.0093 | 0 | 0 |
| g | −2.2586 | 0.204 | −0.2141 |

The viscosity of $H_2O$ is given by correlation (A-16) obtained from [67], where (μ) is in (mPa.s), while T in (K°).

$$\mu_{H_2O} = A.10^{B/T - C} \quad \text{(A-16)}$$

## *A.3. Model parameters: Mass-transfer modeling*

### *A.3.1. $CO_2$ diffusivity in 30 wt% ETA*

It is difficult to determine the diffusivity of $CO_2$ in 30 wt% ETA, due its reactive nature in the solvent. This renders common determination techniques unsuitable. One way of determining this data is by using the $N_2O$ analogy. This analogy - first proposed by Ladda [68] and verified by Joosten [69]– is based on the similarity of molecular sizes between carbon dioxide and dinitrogen monoxide, and states that the ratios of diffusivity and solubility between these molecules is constant irrespective of the solvent. Given that ($N_2O$) does not react with ethanolamine, this relation can be used to estimate the diffusivity of acid gas in a reactive medium as given in:

$$\left[\frac{D_{CO2}}{D_{N2O}}\right]_{H_2O} = \left[\frac{D_{CO2}}{D_{N2O}}\right]_{30\%ETA} \quad \text{(A-17)}$$

The diffusivity of $CO_2$ and $N_2O$ in $H_2O$ were correlated by [70]. They are presented in (A-18) and (A-19) respectively with (T) being the temperature, for a validity range of [273–353 K].

$$D_{CO_2-H_2O} = 3,7191\ 10^{-06}\exp(-2257.9/T) \quad \text{(A-18)}$$

$$D_{N_2O-H_2} = 5,2457\ 10^{-06}\exp(-2388.9/T) \quad \text{(A-19)}$$

Experimental data on the diffusivity of $N_2O$ in aqueous ETA solutions at different temperatures and carbonation ratios are rather very limited and cover the temperature range encountered in the absorption step of carbon capture at null carbonation ratio [54,71,72]. It is for this reason that the diffusivity of $N_2O$ in 30 wt% ETA was determined from the modified Stokes-Einstein equation as shown in (A-20). The exponent value 0.8 was proposed by [70] by fitting experimental data from literature; correlation errors are of the order of 20 % in comparison to experimental data [72].

$$D_{N2O-30\%ETA}\cdot\mu_{30\%ETA}{}^{0,8} = D_{N2O-H2O}\cdot\mu_{H_2O}{}^{0,8} \quad \text{(A-20)}$$

### *A.3.2. ETA diffusivity in 30 wt% ETA solution*

The diffusivity of ETA in aqueous 30 wt%ETA solution was determined from modified Stokes-Einstein correlation presented in (A-21).

$$D_{am}\mu^{0.6}\big|_{H_2O} = D_{am}\mu^{0.6}\big|_{soln} \quad \text{(A-21)}$$

The correlation was fitted by Versteeg [70] to experimental data from literature at 25 °C for different alkanolamines including ETA, (α) was fitted to be 0.6. The diffusivity of the amine in pure water was determined from the Wilke-Change [73] correlation presented in (A-22), with (x) being the molecular weight adjustment factor (1.6 for water), (M) molecular weight of $H_2O$, (T) is the temperature in K°, (μ) is the viscosity of water (mPa.s), and (V) is the molar volume of the solute at its normal boiling point (for ETA 170 °C).

$$D = 7,4.10^{-8}\left[[xM]^{0.5}T\Big/\mu V^{0,6}\right] \quad \text{(A-22)}$$

Snijder [74] measured the diffusivities of alkanolamines in several aqueous alkanolamine solutions at T = [25–60 °C] and that the correlation of Versteeg gave an average error of 7 % and a maximal error of 25 %, while Jamal [72] and Glasscock [75] used the correlation in their studies.

A. Solubility of $CO_2$ in aqueous ETA solution

Versteeg [70] used the $N_2O$ analogy for calculation of $CO_2$ solubility in a reactive medium based on the works of Laddah [68] who found a ratio of solubility between $CO_2$ and $N_2O$ in different organic solvents, and Haimour [76] who verified the validity of the $N_2O$ analogy in aqueous MDEA solution.

The solubility of $CO_2$ and $N_2O$ in pure water were measured and correlated by Jamal [72]. The correlations are shown (A-23), and (A-24) and have a validity range of [273–523 K], as well as [278–393 K] respectively.

$$H(CO2-H_2O) = 10\hat{(}69,395 - 3557,79/T - 22,29\log(T) + 0,0039T) \quad \text{(A-23)}$$

$$H(N2O-H_2O) = 10\hat{(}85,84 - 4373,35/T - 27,71\log(T) + 0,0033T) \quad \text{(A-24)}$$

The ratio of both solubilities is constant as per the $N_2O$ analogy shown in equation (A-25).

$$(H_{CO2}/H_{NO2})_{H2O} = (H_{CO2}/H_{NO2})_{solvent} \quad \text{(A-25)}$$

Wang [77] measured the solubility of $N_2O$ in pure alkanolamines at the temperature range [20–95 °C]. The experimental findings were correlated by (A-26), while coefficients ($b_1$, $b_2$) are presented in Table A5 for several pure alkanolamines. The solubility of $CO_2$ in pure alkanolamines can then be calculated using the $N_2O$ analogy.

$$H_{N2O-am} = b_1\exp(b_2/T) \quad \text{(A-26)}$$

**Table A5**
Coefficients for solubility of $N_2O$ in pure alkanolamines.

| | b1 | b2 | σ (%) |
|---|---|---|---|
| AMP | 86,480 | −1205.2 | 1.55 |
| MEA | 120,700 | −1136.5 | 1.39 |
| DEA | 163,800 | −1174.6 | 2.43 |
| TEA | 482,500 | −1572.2 | 0.3 |
| MDEA | 152,400 | −1312.7 | 0.9 |
| DIPA | 101,000 | −1187.9 | 1.85 |

The solubility of $CO_2$ in a mixture can be determined by (A-27), with ($H_{CO_2,m}$) being the solubility in unloaded solvent mixture, ($\varnothing_i$) being the volumetric fraction of pure solvent (i) in the mixture, ($H_{CO_2,i}$) is the solubility of $CO_2$ in the pure solvent (i), and R is the excess solubility due to the interaction between the different molecules in the mixture.

$$\ln H_{CO_2,m} = \sum \varnothing_i \ln H_{CO_2,i} + R \tag{A-27}$$

The volume fraction of each solvent in the mixture is presented in (A-28), with $v_i$ being the molar volume, and ($x_i$) the molar fraction.

$$\varnothing_i = \frac{x_i v_i}{\sum x_i v_i} \tag{A-28}$$

The excess term (R) was taken from [78,79] and is expressed in (A-29) with ($\alpha_{12}$) being a temperature-dependent empirical parameter obtained from Jamal [72] and valid over the range [20–120 °C].

$$R = \varnothing_1 \varnothing_2 \alpha_{12} \tag{A-29}$$

$$\alpha_{12} = a_1 + a_2/T \tag{A-30}$$

To calculate the solubility of 30 wt% ETA, equation (A-31) can be used. The solubility of $CO_2$ in a solution containing ionic species such as loaded ETA solution, is calculated using (A-31). Here, ($H_{CO_2,m}$) is the solubility in 30 wt% ETA solution with no ionic content, $H^*_{CO_2,m}$ is the solubility of $CO_2$ in a similar solution but with $CO_2$ loading, h is the Van-Krevlen coefficient, and (I) is the ionic strength.

$$\log\left(H^*_{CO_2,m} \Big/ H_{CO_2,m}\right) = hI \tag{A-31}$$

The Van-Krevlen coefficient is expressed in (A-32), with ($h_+$) is the sum of coefficients of cationic species, ($h_-$) that of the ionic species, and ($h_g$) that of dissolved but unreacted gases, i.e. $CO_2$. Coefficients pertaining to the ionic and cationic species were obtained from [80] while that of $CO_2$ was obtained from [81].

$$h = h_+ + h_- + h_g \tag{A-32}$$

The ionic strength (I) is expressed in (A-33) with $c_i$ being the concentration of the ionic species, ($Z_i$) being the charge of the ionic species. Concentrations of ionic species were obtained from Kent-Eisenberg [82] vapor-liquid equilibrium model at 50 °C and were used.

$$I = {}^1\!/_2 \sum c_i Z_i^2 \tag{A-33}$$

### *A.3.3. Diffusivity of $CO_2$ in $N_2$ gas*

The diffusivity of $CO_2$ in $N_2$ gas is calculated from equation (A-34) used by Khaisri [41] with "A" denoting $CO_2$, "B" denotes $N_2$ gas, (M) is the molar mass (g/mol), (T) is the temperature in (°K), (P) is the total pressure (bar), ($\sigma_{AB}$) is the mean collision diameter (Å), ($\Omega$) is the collision integral (unitless). In what follows all expressions and properties were obtained from [83].

$$D_{AB} = \left[0,001858 T^{\frac{3}{2}} (1/M_A + 1/M_B)^{\frac{1}{2}}\right] \Big/ \left[P \sigma_{AB}^2 \Omega_D\right] \tag{A-34}$$

The collision diameter is expressed in (A-35) with ($\sigma_A$) and ($\sigma_B$) corresponding to the molecular diameter of $CO_2$ and $N_2$ respectively. The latter can be calculated from the critical temperature and pressure ($T_c$), and ($P_c$) in (A-36).

$$\sigma_{AB} = [\sigma_A + \sigma_B]/2 \tag{A-35}$$

$$\sigma_A = 2,44 (T_c/P_c)^{1/3} \tag{A-36}$$

The collision integral ($\Omega$) is defined as in equation (A-37), with ($\kappa$) being the Boltzmann constant ($1.38\ 10^{-16}$), and ($\varepsilon_{AB}$) being the energy of molecular interaction for non-binary system defined in (A-38) and (A-39). ($T_b$) is the normal boiling point in kelvin (K°).

$$\Omega = f(\kappa T/\varepsilon_{AB}) \tag{A-37}$$

$$\varepsilon_{AB} = \sqrt{\varepsilon_A \varepsilon_B} \tag{A-38}$$

$$\varepsilon_A/\kappa = 1,15\ T_{b,A} \tag{A-39}$$

The collision integral is identified by the curve shown in Fig. A1.

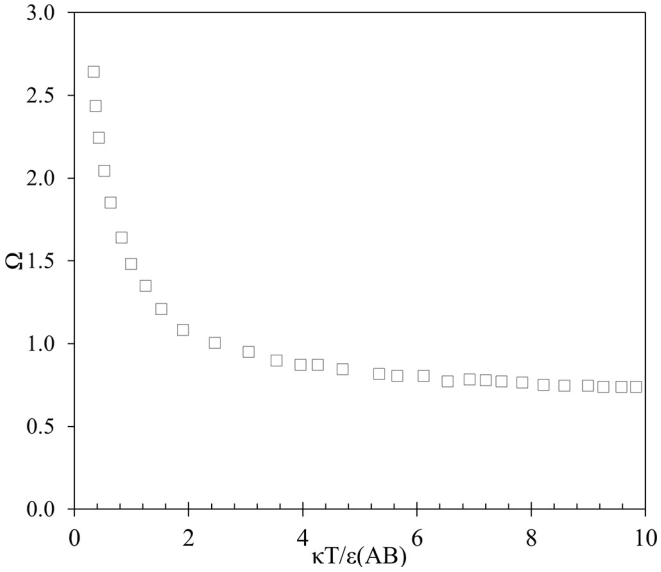



**Fig. A1.** Collision integral for $CO_2$-$N_2$ mixture (Ω)

### *A.3.4. Evaluating the Knudsen diffusivity*

The Knudsen diffusivity was calculated as per the expression from [40–42] and presented in (A-40). "r" is the average pore radius (cm), R is the ideal gas law (8.314 Pa.m$^3$/mol K), T is the temperature (K°), M is the molar weight of $CO_2$.

$$D_{kn} = \frac{2}{3} r \sqrt{8RT/(\pi M_A)} \tag{A-40}$$

Expression (A-40) can be simplified to obtain that more commonly used Eq. (A-41).

$$D_{kn} = 0,97\, r_{pore} \sqrt{T/M_A} \tag{A-41}$$

## Data availability

Data will be made available on request.

## References


[1] K. Calvin, D. Dasgupta, G. Krinner, A. Mukherji, P.W. Thorne, C. Trisos, C. Péan, in: H. Lee, J. Romero (Eds.), IPCC, 2023: climate change 2023: synthesis report. Contribution of working groups I, II and III to the sixth assessment report of the intergovernmental panel on climate change, IPCC, Geneva, Switzerland, 2023, https://doi.org/10.59327/IPCC/AR6-9789291691647. Core writing team. (first.). Intergovernmental panel on climate change (IPCC).

[2] S.A. Kulp, B.H. Strauss, New elevation data triple estimates of global vulnerability to sea-level rise and coastal flooding, Nat. Commun. 10 (1) (2019) 4844, https://doi.org/10.1038/s41467-019-12808-z.

[3] C. Farbotko, Wishful sinking: disappearing islands, climate refugees and cosmopolitan experimentation, Asia Pac. Viewp. 51 (1) (2010) 47–60, https://doi.org/10.1111/j.1467-8373.2010.001413.x.

[4] Paris agreement, UNFCCC, Retrieved from, https://unfccc.int/sites/default/files/english_paris_agreement.pdf, 2018.

[5] P.H.M. Feron, C.A. Hendriks, CO $_2$ capture process principles and costs, Oil Gas Sci. Technol. 60 (3) (2005) 451–459, https://doi.org/10.2516/ogst:2005027.

[6] F. Vega, M. Cano, S. Camino, L.M.G. Fernández, E. Portillo, B. Navarrete, Solvents for carbon dioxide capture, in: I. Karamé, J. Shaya, H. Srour (Eds.), Carbon Dioxide Chemistry, Capture and Oil Recovery. InTech, 2018, https://doi.org/10.5772/intechopen.71443.

[7] D. Singh, E. Croiset, P.L. Douglas, M.A. Douglas, Techno-economic study of CO2 capture from an existing coal-fired power plant: MEA scrubbing vs. O2/CO2 recycle combustion, Energy Convers. Manag. 44 (19) (2003) 3073–3091, https://doi.org/10.1016/S0196-8904(03)00040-2.

[8] C. Alie, L. Backham, E. Croiset, P.L. Douglas, Simulation of CO2 capture using MEA scrubbing: a flowsheet decomposition method, Energy Convers. Manag. 46 (3) (2005) 475–487, https://doi.org/10.1016/j.enconman.2004.03.003.

[9] M.R.M. Abu Zahra, E.S. Fernandez, E.L.V. Goetheer, Guidelines for process development and future cost reduction of CO2 post-combustion capture, Energy Procedia 4 (2011) 1051–1057, https://doi.org/10.1016/j.egypro.2011.01.154.

[10] P. Freund, Making Deep Reductions in CO2 Emissions from Coal- Red Power Plant Using Capture and Storage of CO2, *217*, 2003.

[11] Z. Qi, E.L. Cussler, Microporous hollow fibers for gas absorption: I. Mass transfer in the liquid, J. Membr. Sci. 23 (3) (1985) 321–332, https://doi.org/10.1016/S0376-7388(00)83149-X.

[12] Z. Qi, E.L. Cussler, Microporous hollow fibers for gas absorption: II. Mass transfer across the membrane, J. Membr. Sci. 23 (3) (1985) 333–345, https://doi.org/10.1016/S0376-7388(00)83150-6.

[13] A. Gabelman, S.-T. Hwang, Hollow ®ber membrane contactors, J. Membr. Sci. 46 (1999).

[14] J.-L. Li, B.-H. Chen, Review of CO2 absorption using chemical solvents in hollow fiber membrane contactors, Sep. Purif. Technol. 41 (2) (2005) 109–122, https://doi.org/10.1016/j.seppur.2004.09.008.

[15] Z. Cui, D. deMontigny, Part 7: A review of $CO_2$ capture using hollow fiber membrane contactors, Carbon Manage. 4 (1) (2013) 69–89, https://doi.org/10.4155/cmt.12.73.

[16] A. Mansourizadeh, A.F. Ismail, Hollow fiber gas–liquid membrane contactors for acid gas capture: A review, J. Hazard. Mater. 171 (1) (2009) 38–53, https://doi.org/10.1016/j.jhazmat.2009.06.026.

[17] N. Nishikawa, M. Ishibashi, H. Ohta, N. Akutsu, H. Matsumoto, T. Kamata, H. Kitamura, CO2 removal by hollow-fiber gas-liquid contactor, Energy Convers. Manag. 36 (6–9) (1995) 415–418, https://doi.org/10.1016/0196-8904(95)00033-A.

[18] S. Koonaphapdeelert, Z. Wu, K. Li, Carbon dioxide stripping in ceramic hollow fibre membrane contactors, Chem. Eng. Sci. 64 (1) (2009) 1–8, https://doi.org/10.1016/j.ces.2008.09.010.

[19] G.D. Stefanidis, A.N. Muñoz, G.S.J. Sturm, A. Stankiewicz, A helicopter view of microwave application to chemical processes: reactions, separations, and equipment concepts, Rev. Chem. Eng. 30 (3) (2014), https://doi.org/10.1515/revce-2013-0033.

[20] K. Kranjc, M. Kocevar, From conventional reaction conditions to microwave-assisted catalytic transformations of various substrates. State of the art in 2012 (part B: catalysis), Curr. Org. Chem. 17 (2013) 457–473, https://doi.org/10.2174/1385272811317050004.

[21] K. Kranjc, M. Kocevar, From conventional reaction conditions to microwave-assisted catalytic transformations of various substrates. State of the art in 2012 (part B: catalysis), Curr. Org. Chem. 17 (2013) 457–473, https://doi.org/10.2174/1385272811317050004.

[22] Z. Chemat-Djenni, B. Hamada, F. Chemat, Atmospheric pressure microwave assisted heterogeneous catalytic reactions, Molecules (Basel, Switzerland) 12 (7) (2007) 1399–1409, https://doi.org/10.3390/12071399.

[23] A. Filly, X. Fernandez, M. Minuti, F. Visinoni, G. Cravotto, F. Chemat, Solvent-free microwave extraction of essential oil from aromatic herbs: from laboratory to pilot and industrial scale, Food Chem. 150 (2014) 193–198, https://doi.org/10.1016/j.foodchem.2013.10.139.

[24] D. Zhao, K. An, S. Ding, L. Liu, Z. Xu, Z. Wang, Two-stage intermittent microwave coupled with hot-air drying of carrot slices: drying kinetics and physical quality, Food Bioprocess Technol. 7 (8) (2014) 2308–2318, https://doi.org/10.1007/s11947-014-1274-1.

[25] J.P. Zhang, Y.H. Wu, E.Q. Liu, H. Song, Y. Li, Comparison of storage characteristics and quality of semi-dry fermented sausage using microwave vacuum drying and hot air drying, in: Environmental protection and resources exploitation II 1010, Trans Tech Publications Ltd., 2014, pp. 1783–1788, https://doi.org/10.4028/www.scientific.net/AMR.1010-1012.1783.

[26] P. Guzik, P. Kulawik, M. Zając, W. Migdał, Microwave applications in the food industry: an overview of recent developments, Crit. Rev. Food Sci. Nutr. 62 (29) (2022) 7989–8008, https://doi.org/10.1080/10408398.2021.1922871.

[27] S.J. McGurk, C.F. Martín, S. Brandani, M.B. Sweatman, X. Fan, Microwave swing regeneration of aqueous monoethanolamine for post-combustion CO 2 capture, Appl. Energy 192 (2017) 126–133, https://doi.org/10.1016/j.apenergy.2017.02.012.

[28] F. Bougie, X. Fan, Microwave regeneration of monoethanolamine aqueous solutions used for CO2 capture, Int. J. Greenh. Gas Con. 79 (2018) 165–172, https://doi.org/10.1016/j.ijggc.2018.10.008.

[29] F. Bougie, D. Pokras, X. Fan, Novel non-aqueous MEA solutions for CO2 capture, Int. J. Greenh. Gas Con. 86 (2019) 34–42, https://doi.org/10.1016/j.ijggc.2019.04.013.

[30] A.R. Von Hippel, A.S. Labounsky, Dielectric Materials and Applications, Retrieved from, Artech House, 1995. https://books.google.fr/books?id=qr6mPQAACAAJ.

[31] S.O. Nelson, Correlating dielectric properties of solids and particulate samples through mixture relationships, Transactions of the ASAE 35 (2) (1992) 625–629, https://doi.org/10.13031/2013.28642.

[32] A. STOGRYN, Equations for Calcualting the dielectric constant of saline, Water 19 (8) (1971) 733–736, https://doi.org/10.1109/TMTT.1971.1127617.

[33] A. Hajj, P. Pré, S. Curet, Dielectric dispersion of 30% aqueous monoethanolamine solution loaded with CO2 at microwave frequencies, J. Mol. Liq. 404 (2024) 124819, https://doi.org/10.1016/j.molliq.2024.124819.

[34] RF module- User's guide Comsol. (n.d.). Retrieved from https://doc.comsol.com/6.2/docserver/#!/com.comsol.help.rf/rf_ug_radio_frequency.07.002.html.

[35] L. Graetz, Ueber die Wärmeleitungsfähigkeit von Flüssigkeiten, Ann. Phys. 261 (7) (1885) 337–357, https://doi.org/10.1002/andp.18852610702.

[36] Ibrahim, M. H., El-Naas, M. H., & Zhang, Z. (n.d.). CO2 Capture Using Hollow Fiber Membranes: A Review of Membrane Wetting, 58.

[37] H. Kreulen, C.A. Smolders, G.F. Versteeg, W.P.M. Van Swaaij, Determination of mass transfer rates in wetted and non-wetted microporous membranes, Chem. Eng. Sci. 48 (11) (1993) 2093–2102, https://doi.org/10.1016/0009-2509(93)80084-4.

[38] A. Alkhudhiri, N. Darwish, N. Hilal, Membrane distillation: A comprehensive review, Desalination 287 (2012) 2–18, https://doi.org/10.1016/j.desal.2011.08.027.

[39] M. Fang, Z. Wang, S. Yan, Q. Cen, Z. Luo, CO2 desorption from rich alkanolamine solution by using membrane vacuum regeneration technology, Int. J. Greenh. Gas Con. 9 (2012) 507–521, https://doi.org/10.1016/j.ijggc.2012.05.013.

[40] M. Khayet, M.P. Godino, J.I. Mengual, Modelling transport mechanism through A porous partition, J. Non-Equilib. Thermodyn. 26 (1) (2001) 1–14, https://doi.org/10.1515/JNETDY.2001.001.

[41] S. Khaisri, CO2 stripping from monoethanolamine using a membrane contactor, J. Membr. Sci. 9 (2011).

[42] K. Li, J. Kong, X. Tan, Design of hollow fibre membrane modules for soluble gas removal, Chem. Eng. Sci. 55 (23) (2000) 5579–5588, https://doi.org/10.1016/S0009-2509(00)00193-7.

[43] V.Y. Dindore, D.W.F. Brilman, P.H.M. Feron, G.F. Versteeg, CO2 absorption at elevated pressures using a hollow fiber membrane contactor, J. Membr. Sci. 235 (1–2) (2004) 99–109, https://doi.org/10.1016/j.memsci.2003.12.029.

[44] Chabanon, E. (n.d.). Contacteurs à membranes composites et contacteurs microporeux pour procédés gaz-liquide intensifiés de captage du CO2 en post-combustion: expérimentation et modélisation, 217.

[45] M. Mavroudi, S.P. Kaldis, G.P. Sakellaropoulos, Reduction of CO2 emissions by a membrane contacting process☆, Fuel 82 (15–17) (2003) 2153–2159, https://doi.org/10.1016/S0016-2361(03)00154-6.

[46] M. Rezaei, D.M. Warsinger, V.J.H. Lienhard, M.C. Duke, T. Matsuura, W. M. Samhaber, Wetting phenomena in membrane distillation: mechanisms, reversal, and prevention, Water Res. 139 (2018) 329–352, https://doi.org/10.1016/j.watres.2018.03.058.

[47] R. Wang, D.F. Li, C. Zhou, M. Liu, D.T. Liang, Impact of DEA solutions with and without CO2 loading on porous polypropylene membranes intended for use as contactors, J. Membr. Sci. 229 (1) (2004) 147–157, https://doi.org/10.1016/j.memsci.2003.10.022.

[48] H. Kierzkowska-Pawlak, Determination of kinetics in gas-liquid reaction systems. An overview, Ecol. Chem. Eng. S 19 (2) (2012) 175–196, https://doi.org/10.2478/v10216-011-0014-y.

[49] G. Astarita, D.W. Savage, Gas absorption and desorption with reversible instantaneous chemical reaction, Chem. Eng. Sci. 35 (8) (1980) 1755–1764, https://doi.org/10.1016/0009-2509(80)85011-1.

[50] R.H. Weiland, M. Rawal, R.G. Rice, Stripping of carbon dioxide from monoethanolamine solutions in a packed column, AICHE J. 28 (6) (1982) 963–973, https://doi.org/10.1002/aic.690280611.

[51] K. Zhu, C. Yue, Z. Wei, J. Huang, M. Hu, Y. Ji, Y. Huang, Experimental and thermodynamic investigation on CO2 absorption in aqueous MEA solutions, Adv. Mater. Sci. Eng. 2022 (2022) 6278342, https://doi.org/10.1155/2022/6278342.

[52] A. Barreau, E. Blanchon le Bouhelec, K.N. Habchi Tounsi, P. Mougin, F. Lecomte, Absorption of H $_2$ S and CO $_2$ in alkanolamine aqueous solution: experimental data and modelling with the electrolyte-NRTL model, Oil & Gas Sci. Technol - Revue de l'IFP 61 (3) (2006) 345–361, https://doi.org/10.2516/ogst:2006038a.

[53] M.-H. Li, K.-P. Shen, Calculation of equilibrium solubility of carbon dioxide in aqueous mixtures of monoethanolamine with methyldiethanolamine, Fluid Phase Equilib. 85 (1993) 129–140, https://doi.org/10.1016/0378-3812(93)80008-B.

[54] F.-Y. Jou, A.E. Mather, F.D. Otto, The solubility of CO $_2$ in a 30 mass percent monoethanolamine solution, Can. J. Chem. Eng. 73 (1) (1995) 140–147, https://doi.org/10.1002/cjce.5450730116.

[55] U.E. Aronu, S. Gondal, E.T. Hessen, T. Haug-Warberg, A. Hartono, K.A. Hoff, H. F. Svendsen, Solubility of CO2 in 15, 30, 45 and 60 mass% MEA from 40 to 120°C and model representation using the extended UNIQUAC framework, Chem. Eng. Sci. 66 (24) (2011) 6393–6406, https://doi.org/10.1016/j.ces.2011.08.042.

[56] J.I. Lee, F.D. Otto, A.E. Mather, The solubility of H $_2$ S and CO $_2$ in aqueous monoethanolamine solutions, Can. J. Chem. Eng. 52 (6) (1974) 803–805, https://doi.org/10.1002/cjce.5450520617.

[57] K.P. Shen, M.H. Li, Solubility of carbon dioxide in aqueous mixtures of monoethanolamine with methyldiethanolamine, J. Chem. Eng. Data 37 (1) (1992) 96–100, https://doi.org/10.1021/je00005a025.

[58] C. Zhang, J. Lan, T. Hong, T. Gulati, H. Zhu, Y. Yang, K. Huang, Dynamic analysis and simulation on continuous flow processing of biodiesel production in single-mode microwave cavity, Int. J. Appl. Electromagn. Mech. 51 (2) (2016) 199–213, https://doi.org/10.3233/JAE-160007.

[59] J.A. Reynolds, J.M. Hough, Formulae for dielectric constant of mixtures, Proce. Physical Society. Section B 70 (8) (1957) 769–775, https://doi.org/10.1088/0370-1301/70/8/306.

[60] R. Buchner, G.T. Hefter, P.M. May, Dielectric relaxation of aqueous NaCl solutions, Chem. Eur. J. 103 (1) (1999) 1–9, https://doi.org/10.1021/jp982977k.

[61] Nayef Ghasem, Nihmiya Abdul Rahim, Mohamed Al-Marzouqi, Thermal conductivity of aqueous solvents used in CO2 capture, J. Chemical Eng. Res. Updates 3 (1) (2016) 25–30, https://doi.org/10.15377/2409-983X.2016.03.01.2.

[62] M. Shokouhi, A.H. Jalili, F. Samani, M. Hosseini-Jenab, Experimental investigation of the density and viscosity of CO2-loaded aqueous alkanolamine solutions, Fluid Phase Equilib. 404 (2015) 96–108, https://doi.org/10.1016/j.fluid.2015.06.034.

[63] Thermal conductivity of distilled water. (n.d.). Retrieved from, in: https://powderprocess.net/Tools_html/Data_Diagrams/Water_Properties_Correlations.html.

[64] S.H. Yun, Y.E. Kim, J.H. Choi, S.C. Nam, J. Chang, Y.I. Yoon, CO2 absorption, density, viscosity and vapor pressure of aqueous potassium carbonate+2-methylpiperazine, Korean J. Chem. Eng. 33 (12) (2016) 3473–3486, https://doi.org/10.1007/s11814-016-0210-7.

[65] R.H. Weiland, J.C. Dingman, D.B. Cronin, Heat capacity of aqueous Monoethanolamine, diethanolamine, *N* -Methyldiethanolamine, and *N* -Methyldiethanolamine-based blends with carbon dioxide, J. Chem. Eng. Data 42 (5) (1997) 1004–1006, https://doi.org/10.1021/je960314v.

[66] R.H. Weiland, J.C. Dingman, D.B. Cronin, G.J. Browning, Density and viscosity of some partially carbonated aqueous alkanolamine solutions and their blends, J. Chem. Eng. Data 43 (3) (1998) 378–382, https://doi.org/10.1021/je9702044.

[67] Viscosity of pure water. (n.d.). Retrieved from Source: https://www.engineersedge.com/physics/water_density_viscosity_specific_weight_13146.htm.

[68] S.S. Laddha, J.M. Diaz, P.V. Danckwerts, The N20 analogy the solubaities of CO2 and N20 in aqueous solutions of organic compounds 36, 1981, p. 228.

[69] G.E.H. Joosten, P.V. Danckwerts, Solubility and diffusivity of nitrous oxide in equimolar potassium carbonate-potassium bicarbonate solutions at 25.Deg. and 1 atm, J. Chem. Eng. Data 17 (4) (1972) 452–454, https://doi.org/10.1021/je60055a016.

[70] G.F. Versteeg, W.P.M. Van Swaaij, Solubility and diffusivity of acid gases (carbon dioxide, nitrous oxide) in aqueous alkanolamine solutions, J. Chem. Eng. Data 33 (1) (1988) 29–34, https://doi.org/10.1021/je00051a011.

[71] E. Sada, H. Kumazawa, M.A. Butt, Solubility and diffusivity of gases in aqueous solutions of amines, J. Chem. Eng. Data 23 (2) (1978) 161–163, https://doi.org/10.1021/je60077a008.

[72] A. Jamal, Absorption And Desorption Of C 0 2 And Co In Alkan Olamine Systems, 2025, p. 380.

[73] C.R. Wilke, P. Chang, Correlation of diffusion coefficients in dilute solutions, AICHE J. 1 (2) (1955) 264–270, https://doi.org/10.1002/aic.690010222.

[74] E.D. Snijder, M.J.M. te Riele, G.F. Versteeg, W.P.M. van Swaaij, Diffusion coefficients of several aqueous alkanolamine solutions, J. Chem. Eng. Data 38 (3) (1993) 475–480, https://doi.org/10.1021/je00011a037.

[75] Davide Glasscock, A., August, The university of Texas at Austin, Modelling and experimental study of carbon dioxide absorption into aqueous alkanolamines, 1990.

[76] N. Haimour, O.C. Sandall, Absorption of carbon dioxide into aqueous methyldiethanolamine, Chem. Eng. Sci. 39 (12) (1984) 1791–1796, https://doi.org/10.1016/0009-2509(84)80115-3.

[77] Y.W. Wang, S. Xu, F.D. Otto, A.E. Mather, Solubility of N2O in alkanolamines and in mixed solvents, The Chemical Eng. J. 48 (1) (1992) 31–40, https://doi.org/10.1016/0300-9467(92)85004-S.

[78] T. Boublík, E. Hála, Solubility of gases in mixed solvents, Collect. Czechoslov. Chem. Commun. 31 (4) (1966) 1628–1635, https://doi.org/10.1135/cccc19661628.
[79] G.M. Schneider, J. M. Prausnitz: Molecular Thermodynamics of Fluid Phase Equilibria. International Series in the Physical and Chemical Engineering Sciences. Prentice-Hall Inc., Englewood Cliffs, New Jersey, 1969. 523 Seiten Preis: 145 s, Ber. Bunsenges. Phys. Chem. 74 (3) (1970) 308, https://doi.org/10.1002/bbpc.19700740327.
[80] G.J. Browning, R.H. Weiland, Physical solubility of carbon dioxide in aqueous alkanolamines via nitrous oxide analogy, J. Chem. Eng. Data 39 (4) (1994) 817–822, https://doi.org/10.1021/je00016a040.
[81] K. Onda, E. Sada, T. Kobayashi, S. Kito, K. Ito, Salting-out parameters of gas solubility in aqueous salt solutions, J. Chem. Eng. Jpn 3 (1) (1970) 18–24, https://doi.org/10.1252/jcej.3.18.
[82] R.L. Kent, B. Eisenberg, Better data for amine treating, 87–90, 1976.
[83] J.R. Welty, R.E. Wilson, G. Rorrer, Fundamentals of Momentum, John Wiley & Sons, Heat and Mass Transfer, 2001.

## Glossary

***Notations:***
*E:* Electric field intensity (V/m)
*H:* Magnetic field intensity (A/m)
*ω:* Angular frequency (rd/s)
*μ:* Magnetic permeability (H/m)
*ε:* Electric permittivity (F/m)
$\varepsilon'$*:* Relative permittivity
$\varepsilon''$*:* Dielectric loss factor
*σ:* Electrical conductivity (S/m)
*c:* Speed of light in vacuum (m/s)
*f:* Frequency (Hz)
*λ:* Wavelength (m)
$S_{11}$*:* Reflected power coefficient (dB or %)
*P:* Power (W) or pressure (kPa)
*α:* Carbonation ratio
*r:* Fiber radius (mm)
*a:* Width of WR340 waveguide (43 mm)
*b:* Length of WR340 waveguide (86 mm)
*ρ:* Fluid density (g/mL)
*v:* Fluid velocity (m/s)
*g:* Gravitational acceleration ($m/s^2$)
*μ:* Viscosity (cP)
$C_p$*:* Specific heat (J/g K)
*T:* Temperature (°C)
*Q:* Volumetric heating rate ($W/m^3$)
$\varepsilon_0$**:* Permittivity of free space (F/m)
$\vec{n}$*:* Normal vector
*C:* Concentration ($Mol/m^3$)
*N:* Mass-transfer rate (Mol/s)
*A:* Mass-transfer area ($m^2$)
$He_c$*:* Partition coefficient
*He:* Henry's law (kPa $m^3$ / Mol)
*d:* Diameter (m)
*K:* Overall mass-transfer coefficient (m/s)
*L:* Fiber length (m)
*ξ:* Fiber porosity
*Re:* Reynold's number
*Sc:* Schmidt number
*Sh:* Sherwood number
*D:* Diffusivity ($m^2/s$)
*τ:* Tortuosity
*δ:* Membrane thickness (m)
*M:* Molar mass (g/Mol)
*R:* Ideal gas constant (J/Mol K) or mass-transfer resistance (s/m)
*F:* Wetting fraction
$E_{rxn}$*:* Enhancement factor
*K:* Equilibrium constant of $CO_2$ with ETA
$G_s$*:* Inert gas flow rate (Mol/s)
$L_s$*:* Inert liquid flow rate (Mol/s)
*x:* Mole fraction in liquid phase
*y:* Mole fraction in gas phase
*J:* $CO_2$ desorption flux ($Mol/m^2$ s)
*X:* Mole fraction relative to inert species in liquid phase
*Y:* Mole fraction relative to inert species in gas phase
***Abbreviations:***
*MW:* Microwaves
*EM:* Electromagnetic
*SSC:* Sliding short circuit
*TE:* Transverse electric
*PTFE:* Polytetrafluoroethylene
*DW:* Distilled water
*ETA:* Ethanolamine
*Max:* Maximal
*VNA:* Vector network Analyzer
$CO_2$*:* Carbon dioxide
$N_2$*:* Nitrogen
*Eff:* Effective
*Kn:* Knudsen
*Exp:* Experiment
***Subscripts / superscripts:***
*s:* Phasor domain
*r:* Reflected
*i:* Incident, or at gas-liquid interface
**:* In equilibrium with vapor phase
*l:* Liquid
*m:* Membrane
*k:* Mass transfer coefficient (m/s)
*t:* Total
*f:* Free
*0:* At initial conditions
*R:* Relative
*s:* Phasor domain
*r:* Reflected
*i:* Incident, or at gas-liquid interface
**:* In equilibrium with vapor phase
*l:* Liquid
*g:* Gas